Monthly Notices of the ROYAL ASTRONOMICAL SOCIETY

MNRAS **508,** 1084–1101 (2021) https://doi.org/10.1093/mnras/stab2495
Advance Access publication 2021 September 3

Hardness of ionizing radiation fields in MaNGA star-forming galaxies

Nimisha Kumari [1]★ Ricardo Amorín [2,3]★ Enrique Pérez-Montero,[4] Jose Vílchez [4] and Roberto Maiolino[5,6]

[1]*AURA for the European Space Agency (ESA), Space Telescope Science Institute, 3700 San Martin Drive, Baltimore, MD 21218, USA*
[2]*Departamento de Astronomía, Universidad de La Serena, Av. Juan Cisternas 1200 Norte, La Serena, Chile*
[3]*Instituto de Investigación Multidisciplinar en Ciencia y Tecnología, Universidad de La Serena, Raúl Bitrán 1305, La Serena, Chile*
[4]*Instituto de Astrofísica de Andalucía, CSIC, Apartado de correos 3004, E-18080 Granada, Spain*
[5]*Kavli Institute for Cosmology, University of Cambridge, Cambridge CB3 0HA, UK*
[6]*Cavendish Laboratory, University of Cambridge, Cambridge CB3 0HE, UK*

Accepted 2021 August 16. Received 2021 August 16; in original form 2021 January 22

ABSTRACT

We investigate radiation hardness within a representative sample of 67 nearby ($0.02 \lesssim z \lesssim 0.06$) star-forming (SF) galaxies using the integral field spectroscopic data from the MaNGA survey. The softness parameter $\eta = \frac{O^+/O^{2+}}{S^+/S^{2+}}$ is sensitive to the spectral energy distribution of the ionizing radiation. We study η via the observable quantity η' ($=\frac{[\mathrm{O\,II}]/[\mathrm{O\,III}]}{[\mathrm{S\,II}][\mathrm{S\,III}]}$). We analyze the relation between radiation hardness (traced by η and η') and diagnostics sensitive to gas-phase metallicity, electron temperature, density, ionization parameter, effective temperature, and age of ionizing populations. It is evident that low metallicity is accompanied by low log η', i.e. hard radiation field. No direct relation is found between radiation hardness and other nebular parameters though such relations cannot be ruled out. We provide empirical relations between log η and strong emission line ratios N_2, O_3N_2, and Ar_3O_3, which will allow future studies of radiation hardness in SF galaxies where weak auroral lines are undetected. We compare the variation of [O III]/[O II] and [S III]/[S II] for MaNGA data with SF galaxies and H II regions within spiral galaxies from literature and find that the similarity and differences between different data set are mainly due to the metallicity. We find that predictions from photoionization models considering young and evolved stellar populations as ionizing sources in good agreement with the MaNGA data. This comparison also suggests that hard radiation fields from hot and old low-mass stars within or around SF regions might significantly contribute to the observed η values.

Key words: galaxies: active – galaxies: ISM.

1 INTRODUCTION

An in-depth analysis of star-forming (SF) galaxies requires the characterization of the interstellar medium (ISM) in galaxies, which constitutes matter and radiation field. While the matter is composed of gas and dust, the radiation is produced by both stars and the interstellar matter. The hardness and intensity of radiation field are the fundamental parameters that affect the overall shape of the spectrum of a region consisting of stars and ionized gas. The hardness of ionizing radiation field has been studied via different definitions in different works (e.g. Vilchez & Pagel 1988; Morisset et al. 2016; Nakajima et al. 2018; Pérez-Montero et al. 2020). More fundamentally, radiation hardness is the shape of the spectral energy distribution (SED) or the slope of the extreme ultraviolet spectrum (see e.g. Kewley et al. 2015; Nakajima et al. 2018) and hence can be probed by the effective temperature ($T_{\rm eff}$) of stars producing ionizing photons (e.g. Vilchez & Pagel 1988; Steidel et al. 2014). The ratio of photons capable of ionizing neutral hydrogen (H^0) and helium (He^0), i.e. $Q_{0/1}$ is also used to probe radiation hardness (Morisset et al. 2016). In photoionization models, it is assumed that radiation hardness (parametrized by $T_{\rm eff}$ or stellar population distribution and age), ionization parameter $\mathcal{U}$[1], and chemical abundance of ionized gas are independent quantities that affect the output spectrum of a photoionized nebulae. Steidel et al. (2014) state that the more generalized form of ionization parameter Γ[2] depends on radiation hardness, because the number of hydrogen-ionizing photons can be changed by changing the shape or intensity of ionizing radiation (Kewley et al. 2006). Hence, the hardness of radiation field may be related to various parameters such as initial mass function, age of the stellar population, equivalent effective temperature, and ionization parameter and metallicity, and can be probed via emission lines emanating from the ionized gas component of the ISM.

Collisionally excited emission lines (CELs) in optical wavelength range (e.g. [O II] and [O III]) are widely used to study the properties of the ISM. However, only a few works have also explored the use of near-infrared (NIR) CELs such as [S III] λλ9069, 9532 (see e.g. Vilchez & Pagel 1988; Vilchez & Esteban 1996; Díaz & Pérez-Montero 2000; Pérez-Montero & Díaz 2005; Stasińska 2006; Pérez-

★ E-mail: kumari@stsci.edu (NK); ramorin@dfuls.cl (RA)

[1] $\mathcal{U} = \frac{Q}{4\pi r^2 n_{\rm e}}$ for a spherical H II region, where Q is the rate at which stars produce Lyman continuum photons, r is the distance from the central star or stellar clusters, and $n_{\rm e}$ is the volume density of neutral or ionized hydrogen.
[2] $\Gamma = \frac{n_\gamma}{n_{\rm e}} \approx \frac{n_\gamma}{n_{\rm H}}$ where $n_{\rm H}$ is the number density of hydrogen atoms and n_γ is the equivalent density hydrogen ionizing photons.

Montero & Vílchez 2009; Fernández et al. 2018; Mingozzi et al. 2020; Pérez-Montero et al. 2020) mainly due to the following two reasons. First, only a few spectrographs used in galaxy surveys include useful wavelengths above 9000 Å. Secondly, the NIR wavelength range is strongly affected by telluric absorption and sky lines thus complicating the analysis of these sulphur emission lines. None the less, these lines have enormous potential for determining the characteristic properties of ionized gas from which they emanate. For example, the emission line ratios involving [S III] λ9069, such as S_{23} = [S III] λλ9069, 9532 + [S II] λλ 6717, 6731)/H β and S_3O_3 = [S III] λλ9069, 9532/[O III] λλ4959, 5007 have been proposed as metallicity diagnostics (see e.g. Díaz & Pérez-Montero 2000; Pérez-Montero & Díaz 2005; Stasińska 2006). Similarly, the emission line ratios involving sulphur lines, [S II] λλ6717, 6731/H α versus [S III] λλ9069, 9532/H α, are also proposed to identify the ionization mechanisms in the Low Ionization Nuclear Emission Regions (LINERs, Diaz, Pagel & Wilson 1985). The photoionization models have shown that the line ratio [S II] λλ 6717, 6731/[S III] λλ9069, 9532 is a good indicator of ionization parameter (Mathis 1985; Diaz et al. 1991; Morisset et al. 2016; Kewley, Nicholls & Sutherland 2019), which is critical in understanding the state of plasma in an H II region. Mathis (1982) and Mathis (1985) further pointed out the importance of sulphur lines such as [S III] λ9069, 9532 to determine the relative temperatures of hot stars within nebulae by comparing observations with nebular models on the S^+/S^{++} versus O^+/O diagram. Vilchez & Pagel (1988) modified the procedure from Mathis (1982) and introduced the so-called softness parameter

$$\eta = \frac{O^+/O^{2+}}{S^+/S^{2+}}. \quad (1)$$

η is sensitive to the SED of the ionizing radiation because of the large difference in the ionization potentials of O^+ (35.1 eV) and S^+ (23.2 eV) (Bresolin, Kennicutt & Garnett 1999; Pérez-Montero & Vílchez 2009). However, η is not a directly observable quantity and can be studied via the observable line ratio η' which, in optical, is defined as

$$\eta' = \frac{[\mathrm{O\,II}]\lambda3727/[\mathrm{O\,III}]\lambda\lambda4959, 5007}{[\mathrm{S\,II}]\lambda\lambda6717, 6731/[\mathrm{S\,III}]\lambda\lambda9069, 9532}. \quad (2)$$

The mid-infrared fine structure lines of Ne, Ar, and S are also used to determine η (see e.g. Martín-Hernández et al. 2002; Morisset et al. 2004; Pérez-Montero & Vílchez 2009). The softness parameter η is related η' and electron temperature (T_e) as proposed by Vilchez & Pagel (1988). The following revised relation is obtained using PYNEB and its default values for atomic data:

$$\log \eta = \log \eta' + \frac{0.16}{t} + 0.22, \quad (3)$$

where $t = T_e([\mathrm{O\,III}])/10^4$.

The η' parameter has been used to study the ionization structure and the relative hardness of the ionizing sources in the H II regions within the Milky Way and Magellanic Clouds (Martín-Hernández et al. 2002; Morisset et al. 2004) in the SF galaxies (Hägele et al. 2006; Kehrig et al. 2006; Hägele et al. 2008; Pérez-Montero et al. 2020) and the radial variation of the hardness of the ionizing radiation of H II regions in the discs of spiral galaxies (Pérez-Montero & Vílchez 2009; Pérez-Montero, García-Benito & Vílchez 2019). However, it is important to consider other variables while interpreting η' as radiation hardness. For example, $\log \eta'$ is inversely proportional to equivalent effective temperature ($T_{\rm eff}$ Kennicutt et al. 2000), and $\log \eta$ can be expressed as a linear function of $1/T_{\rm eff}$ (Vilchez & Pagel 1988) for a blackbody spectrum. Similarly, $\log \eta$ and $\log \eta'$ may also be related to nebular parameters such as metallicity (Morisset et al. 2004) and ionization parameter (Pérez-Montero & Vílchez 2009; Fernández-Martín et al. 2017).

Previous studies of η using long-slit or fibre spectra have been limited to a small number of local ($z \sim 0$) galaxies (Hägele et al. 2006, 2008) due to the limitations of spectrographs to reach $\lambda > 9000$ Å. The data obtained from spectrographs like that of Sloan Digital Sky Survey (SDSS) typically cover 3800–9200 Å, which cover [S III] λ9069 up to only a redshift of 0.01 and do not cover [O II] λ3727 required for studying η'. In addition, previous long-slit spectra lack spatially resolved information. In comparison to global galaxy-scale analysis, a spatially resolved investigation provides insight into the local environment within nebulae. Integral field spectroscopy (IFS) is the best available technique to carry out such a study as it allows us to map various properties encoded in the emission lines emanating from the ionized gas component of the ISM within galaxies, thus facilitating studies of correlations between hardness of radiation fields and nebular and stellar properties at local scales. Zinchenko et al. (2019) utilized the IFS data from the Calar Alto Legacy Integral Field Area (CALIFA, Sánchez et al. 2012) survey and performed an indirect study of radiation field hardness at local scales by analyzing the relation between equivalent effective temperature (from [O II] and [O III] lines), ionization parameter, and oxygen abundance. Since the [S III] lines lie beyond the wavelength range of CALIFA, their lack thereof prevented this study to break the degeneracy between radiation hardness and the ionization parameter (see equation 2). Moreover, the results of Zinchenko et al. (2019) are derived and hence applicable to a restrictive sample of H II regions within spiral galaxies. The metallicity estimates in their work are based on strong line methods rather than the robust direct T_e method because the CALIFA survey is not sensitive enough to detect the weak auroral lines within high-metallicity environments.

This work is the first spatially resolved study of η and η' on a large sample of 67 SF galaxies, aimed at understanding the relation between various nebular parameters and the hardness of radiation field at local scales. In this work, we use data set from the MaNGA survey to address and overcome the issues faced by previous surveys and instruments. MaNGA is best suited for the current analysis as its wavelength range is wide enough to cover the sulphur emission lines [S III] λλ9069, 9532 crucial to this study. The MaNGA survey also allows us to include relatively low-metallicity SF galaxies, which increases our odds to detect and map the auroral line [O III] λ4363 enabling us to map *Te* and study its relation with radiation hardness at spatially resolved scales. Such a detailed study on radiation hardness within local SF galaxies exhibiting a wide range of ionization conditions is imperative to understand various factors that regulate radiation hardness.

The paper is organized as follows. Section 2 describes the data set and the criteria for selecting sample galaxies from the MaNGA survey. In Section 3, we focus on the relation between [O III]/[O II] and [S III]/[S II] and its dependence on several measurables related to gas-phase metallicity, age of stellar population, and ionization parameter. In Section 4, we compare our results with the previous observations and existing photoionization models (see also Appendix A). We also discuss the relation between radiation hardness and helium lines in the handful of galaxies where He II 4686 are detected. Section 5 summarizes our main results. Throughout this study, we use the following shorthand notation for the strong line ratios for a compact presentation:

$$N_2 = \log([\mathrm{N\,II}]/\mathrm{H}\alpha) = \log([\mathrm{N\,II}]\lambda6584/\mathrm{H}\alpha) \quad (4)$$

$$\mathrm{O_3N_2} = \log((\mathrm{[O\,III]}/H\beta)/(\mathrm{[N\,II]}/H\alpha)) = \log((\mathrm{[O\,III]}\lambda5007/H\beta)/(\mathrm{[N\,II]}\lambda6584/H\alpha)) \quad (5)$$

$$\mathrm{O_3O_2} = \log(\mathrm{[O\,III]}/\mathrm{[O\,II]}) = \log(\mathrm{[O\,III]}\lambda\lambda4959, 5007/\mathrm{[O\,II]}\lambda3727) \quad (6)$$

$$\mathrm{S_3S_2} = \log(\mathrm{[S\,III]}/\mathrm{[S\,II]}) = \log(\mathrm{[S\,III]}\lambda\lambda9069, 9532/\mathrm{[S\,II]}\lambda\lambda6717, 6731) \quad (7)$$

$$\mathrm{S_3O_3} = \log(\mathrm{[S\,III]}/\mathrm{[O\,III]}) = \log(\mathrm{[S\,III]}\lambda\lambda9069, 9532/\log(\mathrm{[O\,III]}\lambda\lambda4959, 5007) \quad (8)$$

$$\mathrm{Ar_3O_3} = \log(\mathrm{[Ar\,III]}/\mathrm{[O\,III]}) = \log(\mathrm{[Ar\,III]}\lambda\lambda7135/\log(\mathrm{[O\,III]}\lambda\lambda4959, 5007) \quad (9)$$

$$\mathrm{S_{23}} = \log((\mathrm{[S\,III]} + \mathrm{[S\,II]})/H\beta) = \log((\mathrm{[S\,III]}\lambda\lambda9069, 9532 + \mathrm{[S\,II]}\lambda\lambda6717, 6731)/H\beta) \quad (10)$$

$$\mathrm{R_{23}} = \log((\mathrm{[O\,III]} + \mathrm{[O\,II]})/H\beta) = \log((\mathrm{[O\,III]}\lambda\lambda4959, 5007 + \mathrm{[O\,II]}\lambda3727)/H\beta) \quad (11)$$

In this paper, we adopt a standard cosmology assuming the parameters, $H_0 = 67.3 \pm 1.2\,\mathrm{km\,s^{-1}\,Mpc^{-1}}$ and $\Omega_\mathrm{m} = 0.315 \pm 0.017$, presented by Planck Collaboration (2014) and are consistent with Planck Collaboration (2016).

2 GALAXY SAMPLE AND DATA

2.1 Galaxy sample

We analyze the IFS data of a sample of 67 SF galaxies observed as a part of MaNGA survey (Bundy et al. 2015). Observations were taken with the Baryonic Oscillation Spectroscopic Survey spectrographs (Smee et al. 2013) on the SDSS 2.5-m telescope (Gunn et al. 2006) at the Apache Point Observatory. The MaNGA data cover a wavelength range of 3600–10300 Å and have a spectral resolution $R \sim 2000$ corresponding to the instrumental full width at half-maximum (FWHM) ∼70 km s^{-1} at the Hα emission line. The reduced data cubes have the spatial sampling of 0.5 arcsec and the effective spatial resolution of ∼2.5 arcsec FWHM. See Yan et al. (2016) for the survey design, Law et al. (2015) for observing strategy, and Law et al. (2016) for data reduction pipeline.

The sample of 67 SF galaxies is a subset of a larger sample of ∼1400 galaxies in MaNGA data set from Data Release 14 (DR14)[3], which include SF galaxies, active galactic nuclei (AGNs), and LINERs with reliable [S III] line detections in the redshift range of 0.02–0.06 (Amorin et al., in preparation). Since these analyses depend on the use of [S III] lines, the redshift cuts are imposed in the parent sample so that at least one of the two [S III] λλ9069,9531 lines lies outside the wavelength range of 9300–9700 Å, which is most affected by a strong telluric absorption band. To address this issue, we include only those galaxies for which the emission line ratio [S III]λ9069/9532 has a maximum deviation of 50 per cent of the theoretical line ratio (= 2.5, Fischer, Tachiev & Irimia 2006) for all spaxels with signal-to-noise (S/N) ratio of >3.

For the current sample, we define a galaxy as SF if the emission line ratios of the central 2.5-arcsec fibre region of the galaxy fall in the SF region of the classical emission line diagnostic (BPT, Baldwin, Phillips & Terlevich 1981) diagram of [O III]/Hβ versus [N II]/Hα. Fig. 1 shows that the emission line ratios estimated from the central spectrum (2.5 arcsec/diameter) of galaxy sample follow the SF sequence lying below the empirical demarcation line of Kauffmann et al. (2003). One galaxy, MaNGA-8626-12704 (also catalogued as SHOC 579), is an interesting exception, which will be useful to probe more extreme environments. This is a well-known extreme emission-line galaxy (see e.g. Kniazev et al. 2004; Fernández et al. 2018), which falls slightly above (but still consistent within errors) the demarcation lines in the BPT diagrams due to its unusually high ionization properties. Note that similar H II galaxies with high excitation and low metallicity, such as the Green Peas (Cardamone et al. 2009; Amorín, Pérez-Montero & Vílchez 2010), which are known to be local analogues of high-redshift galaxies, often lie in the upper left part of the BPT diagnostics, quite offset with respect to the SF sequence and sometimes exceeding the demarcations set by photoionization models (Pérez-Montero & Contini 2009; Feltre, Charlot & Gutkin 2016; Xiao, Stanway & Eldridge 2018).

Table 1 lists general properties of all sample galaxies along with their plate identifications as mentioned in the DR14 catalogue (Sánchez et al. 2016a,b,c). The sample spans the stellar mass range of $8.53 \lesssim \log(\mathrm{M_\star/M_\odot}) \lesssim 10.05$ and SFR range of $-0.79 \lesssim \log(\mathrm{SFR/M_\odot yr^{-1}}) \lesssim 1.30$. The equivalent width (EW) of Hα of the central spectrum of the sample lies in the range of ∼20–1000 Å, further ensuring that the galaxies are SF. Our selection criteria are intended to assemble a representative sample of SDSS-like SF galaxies along the [N II]-BPT diagram, including galaxies with reliable spaxel data in all the relevant emission lines. Note that our sample is not complete by any means. Mingozzi et al. (2020) present a larger sample of Manga SFGs with [S III] measurements. Figs B1–B3 (Appendix B) show the SDSS cutouts of all 67 galaxies in the sample on which hexagonal field of view (FOV) of MaNGA is overlaid.

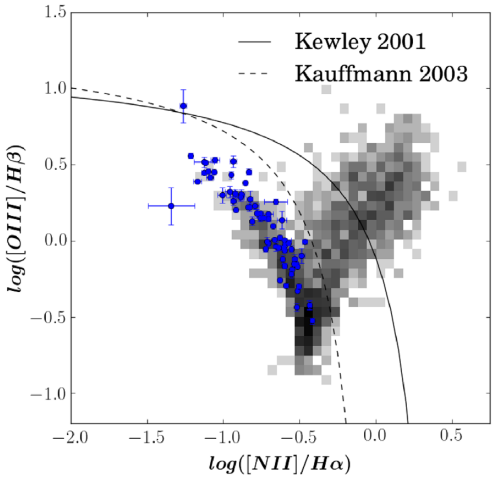

Figure 1. The emission line ratio diagnostic diagram showing [O III]/Hβ versus [N II]/Hα estimated from the central spectra of 67 sample galaxies (blue points). The dashed black curve and the solid black curve represent the empirical Kauffmann line (Kauffmann et al. 2003) and the theoretical maximum starburst Kewley line (Kewley et al. 2001), respectively, used for separating the left star-forming sequence from the right mixing sequence comprising AGN and LINERs. The grey density diagram in the background represents the galaxies in DR14 with finite values of both line ratios, i.e. a total of 2572 galaxies.

[3]https://www.sdss.org/dr14/manga/

Table 1. General properties of sample MaNGA galaxies.

Plate-IFU	RA (J2000)	Dec (J2000)	z	log $M_\star$ ($M_\odot$)	log SFR (H α) ($M_\odot$ yr^{-1})	kpc/arcsec
7495-6102*	204.51292	26.338177	0.0268	8.80	− 0.05	0.56
7975-1901	323.65747	11.421048	0.0227	8.95	− 0.09	0.47
7990-3703	262.09933	57.545418	0.0291	9.68	0.81	0.60
7992-6102	253.88911	63.242126	0.0228	9.36	0.28	0.48
8078-3703	42.387463	− 0.78446174	0.0239	9.28	− 0.35	0.50
8081-3704	49.821426	− 0.9696393	0.0540	9.85	0.97	1.09
8131-9101	112.57339	39.94194	0.0503	9.87	0.87	1.01
8132-3702	110.55611	42.18362	0.0446	9.63	0.21	0.91
8133-3704	112.51493	43.379227	0.0269	8.53	− 0.39	0.56
8241-6101†	127.04849	17.374716	0.0218	8.70	-0.17	0.45

Notes. Table 1 is published in its entirety in the electronic version where we also indicate the galaxies with He II λ4686 and [O III] 4363 detections via † and * symbols, respectively. We show here a part of the table for guiding the users regarding its structure and content. Stellar mass is taken from the MaNGA Firefly VAC (Goddard et al. 2017; Parikh et al. 2018), while rest of the quantities are taken from the Pipe3D VAC.

2.2 Data

For this work, we use data products included in the MaNGA DR14 Pipe3D value added catalogue (VAC)[4] (Sánchez et al. 2016a,b,c). PIPE3D is a spectroscopic analysis pipeline based on a package called FIT3D[5] and is developed to analyze the properties of stellar populations and ionized gas via emission lines in the spatially resolved optical spectra. In short, this pipeline performs continuum fitting on binned spaxels of data cubes using the single stellar population templates from the MIUSCAT library (Vazdekis et al. 2012), which is an extension of MILES library (Sánchez-Blázquez et al. 2006; Vazdekis et al. 2010; Falcón-Barroso et al. 2011). For analyzing strong emission lines, single Gaussian profiles are fit to estimate properties such as flux intensity, velocity, velocity dispersion, and EW. However, the same properties of weak emission lines are based on a direct estimation procedure based on a prior estimate of gas kinematics and Monte Carlo realizations. In addition, stellar indices such as $D_N(4000)$ are also estimated to characterize properties of stellar populations.

We downloaded data products of sample galaxies from the links provided on the MaNGA website[3]. The data products include data cubes, EW maps, and flux maps of emission lines of interest along with their uncertainty maps (see Appendices C and D for some example maps). We perform an S/N cut of 3 on all flux maps for the subsequent analysis. The emission line flux maps available from PIPE3D are corrected for Galactic foreground extinction but not for the internal reddening. We use the extinction curve of Large Magellanic Cloud (Fitzpatrick 1986) and theoretical value of Balmer decrement (H α/H $\beta = 2.86$ assuming electron temperature $T_e = 10^4$ K and electron density $N_e = 100$ cm^{-3}, see e.g. Osterbrock & Ferland 2006) to first estimate the colour excess [i.e. $E(B-V)$] for each galaxy and then combine with the observed flux maps of all emission lines of interest to estimate the extinction-corrected flux maps. A few studies recommend using the closer Paschen lines for estimating reddening correction for [S III] lines (e.g. Pérez-Montero et al. 2019); however, we do not adopt that methodology because Paschen line maps are not available for this sample in the DR14 MaNGA data set. We use the intrinsic flux maps for further analysis except for line ratios with emission lines close in wavelengths. Uncertainties on these intrinsic maps are estimated by propagating errors on the observed flux maps and then on all quantities of interest, for example, the emission line ratios.

We use theoretical line ratios of [O III] λ5007/[O III] λ4959 (= 3, see e.g. Osterbrock & Ferland 2006) and [S III] λ9532/[S III] λ9069 (= 2.5, Fischer et al. 2006) to estimate intrinsic fluxes of emission lines [S III] λ9069 and [O III] λ4959 from [S III] λ9532 and [O III] λ5007, respectively. For this work, we prefer to use [S III] λ9532 instead of [S III] λ9069 because it has better S/N ratio and is generally found outside the wavelength regions most affected by residuals from the telluric absorption correction at the redshift of this sample. It is worth noting that the continuum fitting performed for the Pipe3D MaNGA VAC is found to be highly reliable out to ∼9470 Å. While [S III] λ9069 is mostly within that limit, the [S III] λ9531 is in a wavelength range where the continuum subtraction relies on an extrapolation of the MIUSCAT models beyond 9470 Å. Thus, the [S III] λ9531 may in principle be subject of larger uncertainty. To minimize potential biases, first we have checked that our sample has excellent continuum fitting, i.e. quality flags *QCflag* = 0 in the Pipe3D catalogues, and secondly, our sample selection was constrained to galaxies with spaxel data where the [S III] λ9069/9532 ratio is consistent within 50 per cent with the theoretical ratio. Our tests show that for galaxies with spaxel data with S/N ([S III] λ9531) $\gtrsim$ 10, such consistency is actually better than 15 per cent. Thus, we estimate the relative uncertainty due to continuum subtraction issues to be a factor of 1.5 at most. Overall, this translates into a maximum expected uncertainty of about 0.2 dex for line ratios involving [S III].

2.3 Classical and novel emission line diagnostic diagrams

We use classical and novel emission line diagnostic diagrams to verify that the spaxels used in this analysis are predominantly SF. Fig. 2 shows spatially resolved emission line diagnostic diagrams, [O III]/H β versus [N II]/H α (left-hand panel) and [O III]/H β versus [S II]/H α (right-hand panel). The blue data points correspond to all spaxels considered within the galaxy sample, where the involved emission lines (i.e. H β, [O III] λ5007, [N II] λ6584, H α and [S II] λλ6717, 6731) have an S/N > 3. Superimposed green data points are a subset of blue ones corresponding to those spaxels where the [S III] λ9532 emission line is also detected with S/N > 3. On both panels, black solid curves denote the theoretical maximum starburst line from Kewley et al. (2001). On the left-hand panel, we also

[4] https://www.sdss.org/dr14/manga/manga-data/manga-pipe3d-value-added-catalog/
[5] http://www.astroscu.unam.mx/~sfsanchez/FIT3D

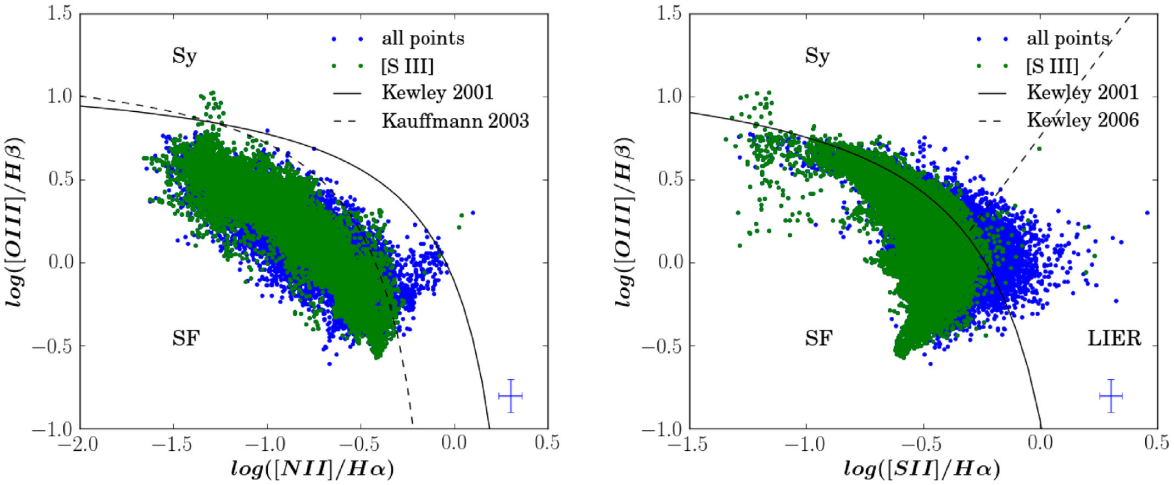

Figure 2. Left-hand panel: [O III]/H β versus [N II]/H α. Right-hand panel: [O III]/H β versus [S II]/H α. On both panels, spatially resolved (spaxel-by-spaxel basis) emission line diagnostic diagrams for all sample galaxies. Blue data points correspond to spatially resolved (spaxel-by-spaxel basis) emission line ratios for all spaxels where all emission lines used in the line ratios on the two axes are detected with S/N > 3, whereas green data points represent a subset of blue data points that show the detection of [S III] λ9532 emission line with S/N > 3. The typical uncertainties on emission line ratios for all data points (i.e. blue data set) are shown in the bottom right corner of each panel. Solid black curve and dashed black curve correspond to the maximum starburst line from Kewley et al. (2001) and Kauffmann et al. (2003), respectively, which provide a classification based on excitation mechanisms. The dashed straight line on the right-hand panel separates Seyferts from LI(N)ERs derived by Kewley et al. (2006). We find that a few green data points lie beyond the Kauffmann line and Kewley line in the left-hand and right-hand panels, respectively. However, the typical uncertainties are large enough for these points to put them in star-forming region of the BPT diagrams.

show a black dashed curve that corresponds to the demarcation line from Kauffmann et al. (2003) derived empirically using $\sim 10^5$ SDSS galaxies. The right-hand panel also shows a dashed straight line separating the spaxels with line ratios exhibited by Seyferts (Sy) and low ionization (nuclear) emission regions [LI(N)ERs, Belfiore et al. 2016]. On both panels, we find that the spatially resolved blue data points not only lie in the SF sequence but also spill into the region beyond the maximum starburst lines. On the contrary, green data points (corresponding to spaxels with [S III] λ9532 detection) appear to lie on the SF sequence better than blue data points. In the following, we solely concentrate on these green data points.

In Fig. 3, the upper panel presents the relations between [O III]/H β versus [N II]/H α (left-hand panel) and [O III]/H β versus [S II]/H α (right-hand panel), and the lower panel presents the relation between [S III]/H α versus [N II]/H α (left-hand panel) and [S III]/H α versus [S II]/H α (right-hand panel). On all panels, data are colour-coded with respect to log EW(H β), which is an age indicator for the young stellar populations (Leitherer et al. 1999). We find that EW(H β) varies with [S II]/H α and [N II]/H α, with high EW regions showing higher excitation and lower [N II]/H α and [S II]/H α, while there is no such trend with respect to [S III]/H α suggesting that [S III]/H α is not correlated with age.

We introduce here novel forms of classical BPT diagrams replacing [O III]/H β with [SIII]/H α, which will serve to classify SF regions from LI(N)ER/Sy-like regions for future studies that lack blue end of optical spectrum. The black curves in Fig. 3 (lower panel) are the maximum starburst curves derived empirically from a larger sample of MaNGA galaxies (Amorin et al., in preparation). The region lying below these curves is dominated by stellar photoionization while the region beyond the curves is mostly ionized by shocks and non-thermal sources. From Fig. 3, we find that a majority of spaxels identified as SF on classical BPT diagrams (upper panel) show similar ionization on the novel [S III]-BPT diagrams (lower panel). The equations for the maximum starburst curve for the novel [S III]-BPT diagnostic diagrams are mentioned as below:

For [S III]/H α versus [N II]/H α (Fig. 3, lower left-hand panel), SF regions satisfy the following relation:

$$\log([\mathrm{S\,III}]/H\alpha) < \frac{0.09}{\log([\mathrm{N\,II}]/H\alpha) - 0.35} - 0.29. \quad (12)$$

For [S III]/H α versus [S II]/H α (Fig. 3, lower right-hand panel), SF regions satisfy the following relations:

$$\log([\mathrm{S\,III}]/\mathrm{H}\alpha) < \frac{0.07}{(\log([\mathrm{S\,II}]/\mathrm{H}\alpha) - 0.22)} - 0.32, \quad \text{for } \log([\mathrm{S\,III}]/\mathrm{H}\alpha) \geq -0.8. \quad (13)$$

$$\log([\mathrm{S\,III}]/\mathrm{H}\alpha) < \frac{-0.34}{(\log([\mathrm{S\,II}]/\mathrm{H}\alpha) - 0.41)} - 1.86, \quad \text{for} -1.4 \leq \log([\mathrm{S\,III}]/\mathrm{H}\alpha) < -0.8. \quad (14)$$

$$\log([\mathrm{S\,II}]/\mathrm{H}\alpha) < -0.32, \text{ for} -2.0 \leq \log([\mathrm{S\,III}]/\mathrm{H}\alpha) < -1.4. \quad (15)$$

3 RESULTS: RELATIONS BETWEEN RADIATION HARDNESS AND FUNDAMENTAL NEBULAR PARAMETERS

Understanding the hardness of the ionizing radiation field is important as, along with nebular geometry and gas density, it determines the ionization structure of an H II region. As explained in Section 1, radiation hardness may correlate with various properties of ionizing stars and ionized nebula such as equivalent effective temperature, stellar age, electron temperature, density, and chemical abundances within a nebula, while nebular structure can be characterized by ionization parameter. In an H II region, the ratio of the number density of ions of same element in successive ionization state (e.g. S^{2+}/S^{+}, O^{2+}/O^{+}) depends on the hardness of the ionizing spectrum and

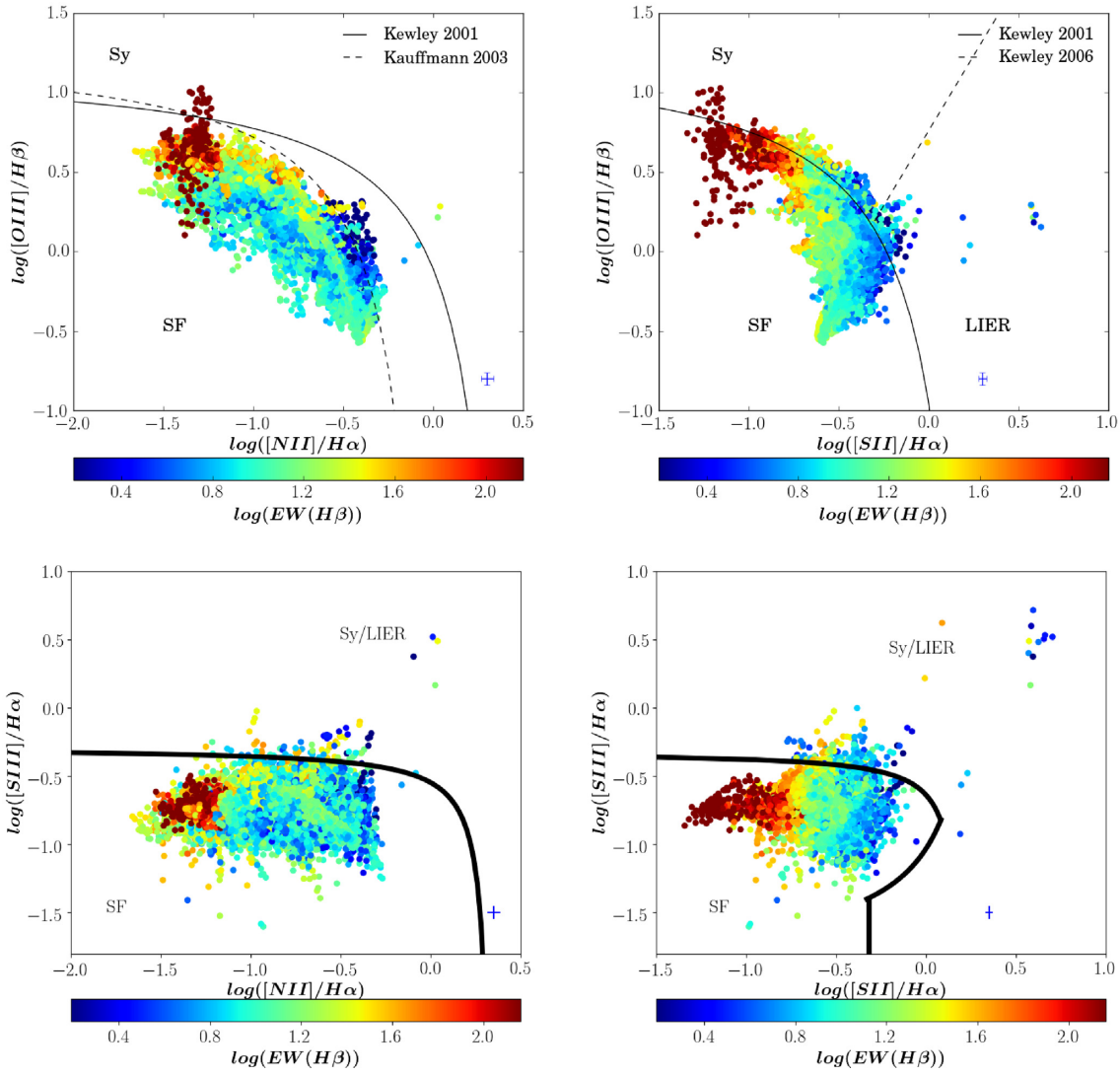

Figure 3. Upper panel: [O III]/H β versus [N II]/H α (left-hand panel) and [O III]/H β versus [S II]/H α (right-hand panel). The solid black curve on both panels corresponds to the maximum starburst line given in Kewley et al. (2001), while the dashed curve on the left-hand panel corresponds to the demarcation line between star-forming and Seyfert galaxies derived by Kauffmann et al. (2003). The dashed line on the right-hand panel separates Seyferts from LI(N)ERs as derived in Kewley et al. (2006). Lower panel: [S III]/H α versus [N II]/H α (left-hand panel) and [S III]/H α versus [S II]/H α (right-hand panel). The black solid curves on the lower panels represent the maximum starburst line derived empirically in Amorin et al. (in preparation) and presented as equations (12)–(15). On all panels, data points represent the spatially resolved emission line ratios in all 67 galaxies but only for those spaxels that have [S III] λ9532 detected with S/N $>$ 3 and are colour-coded with respect to log EW(H β). The typical uncertainties on x- and y-axes are shown in the bottom right corner of each panel. Note that these data points correspond to green data points in classical emission line diagnostic diagrams presented in Fig. 2.

the effective ionization parameter. The emission line ratios such as [O III]/[O II] and [S III]/[S II] are known to be ionization parameter diagnostics (see e.g. Kewley & Dopita 2002; Morisset et al. 2016). Thus, by studying the variation of [O III]/[O II] versus [S III]/[S II] (referred to as O_3O_2–S_3S_2 plane hereafter), we can in principle remove the effects of ionization parameter and study the hardness of radiation field to a first-order approximation (Vilchez & Pagel 1988). In this section, we analyze the O_3O_2–S_3S_2 plane with respect to several other properties that might be related to the hardness of radiation field. We have performed this study on spaxel-by-spaxel basis for individual galaxies as well as for all spaxels combined from all 67 galaxies. We note that, despite some spaxels lie slightly above the SF empirical demarcation lines in the [S II]-BPT diagnostic, the overall results presented in this section remain unchanged if we limit ourselves to those spaxels whose line ratios lie below the maximum theoretical starburst line (Kewley et al. 2001) on [S II]-BPT. In the following, we present the results from the combined sample for all spaxels, though same analysis for five individual galaxies is also presented in Appendix D where [O III] λ4363 detections are spatially extended, enough for a comparison with other line ratios, in particular, log η'. We also note that the spaxels presented in these diagrams are correlated over a few pixels. However, the presence of trends will not be affected by the correlated pixels, though the absence of trends should be interpreted with caution.

3.1 Gas-phase metallicity

Fig. 4 shows the O_3O_2–S_3S_2 plane for spatially resolved data (on spaxel-by-spaxel basis) of all 67 galaxies in the sample where data points are colour-coded with respect to the abundance-sensitive

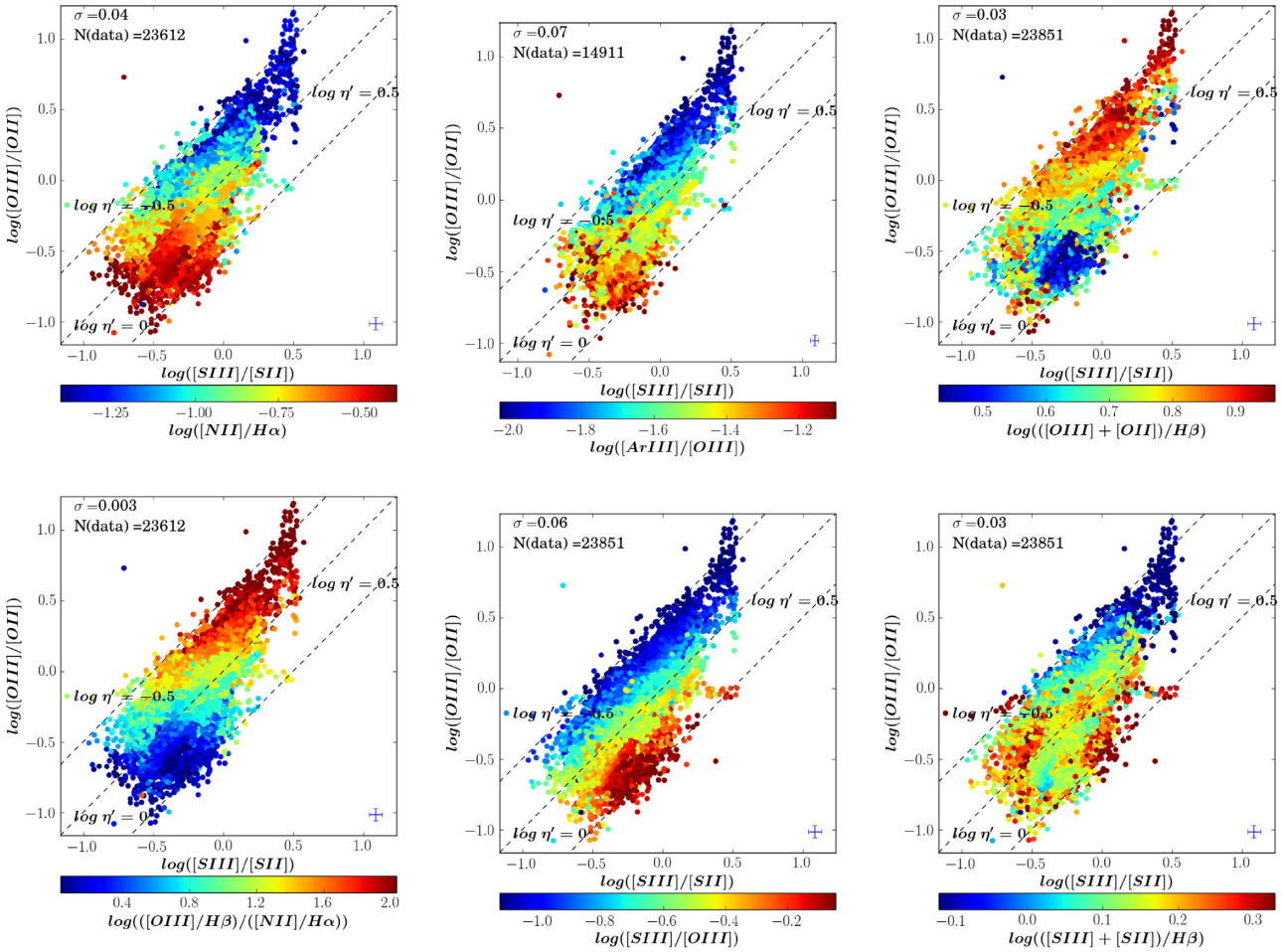

Figure 4. Spatially resolved data of all 67 galaxies plotted on O_3O_2–S_3S_2 plane, where data points are colour-coded with respect to abundance-sensitive emission line diagnostics, N_2 (upper left-hand panel), O_3N_2 (lower left-hand panel), Ar_3O_3 (upper middle panel), S_3O_3 (lower middle panel), R_{23} (upper right-hand panel), and S_{23} (lower right-hand panel). On each panel, the diagonal dashed lines represent the constant values of log $\eta' = -0.5$, 0, 0.5. The typical uncertainties on O_3O_2 and S_3S_2 are shown in the lower right corner of each panel. In the upper left corner of each panel, σ denotes the typical uncertainties on the variable (i.e. N_2, O_3N_2, Ar_3O_3, S_3O_3, S_{32}, and R_{32}) with respect to which data points are colour-coded, and 'N(data)' represents the total number of plotted data points. Note that N(data) in the first two panels is determined by the number of spaxels with enough S/N (>3) for [S III] λ9532 emission line. However, number of spaxels with enough S/N (>3) for [Ar III] λ7135 determines N(data) in the last panels and is significantly lower than the first two panels as [Ar III] λ7135 is more difficult to detect than [S III] λ9532, since the ionization potential of [S III] (34.83 eV) is lower than that of [Ar III] (40.74 eV).

emission line ratios, N_2, O_3N_2, Ar_3O_3, S_3O_3, R_{23}, and S_{23}. On each panel, three diagonal dashed lines correspond to constant values of log $\eta' = -0.5$, 0 and 0.5, where η' is given by equation (2). Note that log $\eta' = 0$ corresponds to spaxels with $O_3O_2 = S_3S_2$. A harder radiation field corresponds to lower values of log η' and vice versa. In the following, we discuss the variation in O_3O_2–S_3S_2 relation with each metallicity diagnostic mentioned above:

(i) **N_2** has been shown to increase with an increase in metallicity (see e.g. Pettini & Pagel 2004; Maiolino et al. 2008; Pérez-Montero & Contini 2009; Marino et al. 2013; Curti et al. 2017; Maiolino & Mannucci 2019) over a wide range of metallicities (7.6 < 12 + log(O/H) < 8.85) though it suffers from saturation of [N II] at higher metallicities. In Fig. 4 (upper left-hand panel), N_2 shows a gradient on O_3O_2–S_3S_2 plane, where it decreases with a decrease in log η'. However, a constant value of log η' does not correspond to a constant value of N_2, which indicates a secondary dependence on other unknown parameters. We find that at a constant S_3S_2, a lower value of N_2, i.e. a lower metallicity corresponds to a harder radiation field and vice versa. However, at a constant O_3O_2, variation of N_2 with hardness of radiation field is less obvious. Both S_3S_2 and O_3O_2 trace ionization parameter (log $\mathcal{U}$), though S_3S_2 is shown to be a better diagnostic of log $\mathcal{U}$ than O_3O_2 (Morisset et al. 2016). Hence, it appears that log η' increases with an increase in metallicity (if traced by N_2) at constant ionization parameter (if traced by S_3S_2).

We also find that the highest values of O_3O_2 correspond to the lowest metallicities at a given value of S_3S_2. This result agrees with the findings of Kehrig et al. (2006) and Stasińska et al. (2015) for local blue compact dwarf galaxies with very high excitation. Moreover, the photoionization models of Kewley & Dopita (2002, Fig. 1) also show an increase in metallicity with a decrease in O_3O_2 at a given ionization parameter (traced by S_3S_2). We will further discuss log η' and ionization parameter in Section 3.3.

(ii) **O_3N_2** is known to decrease with an increase in metallicity (see e.g. Pettini & Pagel 2004; Maiolino et al. 2008; Marino et al. 2013; Curti et al. 2017; Maiolino & Mannucci 2019) and is deemed to be more useful than N_2 in the high-metallicity regime, where [N II] saturates but the strength of [O III] continues to decrease with

metallicity. In Fig. 4 (lower left-hand panel), O_3N_2 shows a similar gradient as seen in the case of N_2, indicating that metallicity and log η' are correlated.

(iii) **Ar_3O_3** follows a monotonically increasing relation with the electron temperature and hence with the metallicity (Stasińska 2006). It is considered to be a more accurate metallicity diagnostic than N_2 at higher metallicity but needs a reliable reddening correction (unlike N_2). Moreover, it is unaffected by the presence of diffuse ionized gas (DIG) because of the use of high excitation lines and not the low excitation lines, which may arise in both H II regions and DIG. In Fig. 4, we study O_3O_2–S_3S_2 plane where data points are colour-coded with respect to Ar_3O_3 ratio, where higher Ar_3O_3 indicates higher metallicity. We find a similar gradient as N_2 and O_3N_2 though we note a weaker trend at lower values of O_3O_2 and S_3S_2, which might be simply because of fewer spaxels with enough S/N (>3) of [Ar III] λ7135.

(iv) **S_3O_3** is posed as a good diagnostic of metallicity in both low- and high-metallicity regimes, which like Ar_3O_3, is unaffected by the presence of DIG (Stasińska 2006). Hence, we explored O_3O_2–S_3S_2 plane with a third variant as S_3O_3 line ratio in Fig. 4 (lower middle panel). We find a clear gradient in S_3O_3 across log $\eta' = -0.5$–0.5, where S_3O_3 appears to be approximately constant at a given value of log η' unlike our observation in previous plots. Note here that it might be simply because emission lines ([S III] and [O III]) involved in this metallicity diagnostic appear in the numerators of two axes on this plane, while the effects of the two emission lines in the denominator (i.e. [S II] and [O II]) nullify because of their very similar ionization potentials and probably because oxygen and sulphur are produced in similar stars. We should therefore be cautious while using S_3O_3 as a metallicity indicator on the O_3O_2–S_3S_2 plane because the involved emission lines appear to be more sensitive to hardness of radiation fields.

(v) **R_{23}** traces metallicity but there are two major caveats in its use: first, it is bimodal with metallicity, and secondly, it also depends on ionization parameter (see e.g. Kewley & Dopita 2002). This means that one needs to determine the metallicity regime (low or high) as well as ionization parameter to use R_{23} for inferring a reliable value of metallicity. In Fig. 4 (upper right-hand panel), we find that the variation of R_{23} on the O_3O_2–S_3S_2 plane is similar to other metallicity diagnostics though the trend is less obvious for lower values of O_3O_2 and S_3S_2. For example, at a constant value of $S_3S_2 = -0.5$, there is practically no trend in R_{23}. It is possible that the metallicites of these spaxels lie in the 'knee', a region of confusion (i.e. 12 + log(O/H) ∼8.1–8.3) where R_{23} peaks.

(vi) **S_{23}** has been used to trace metallicity (Vilchez & Esteban 1996; Pérez-Montero & Díaz 2005; Hägele et al. 2006; Kehrig et al. 2006) and is similar to the R_{23} parameter; however, the knee (i.e. metallicity regime of confusion) appears at a higher metallicity (12 + log(O/H) ∼ 8.8, Kewley & Dopita 2002) than R_{23}. In Fig. 4 (lower right-hand panel), we do not observe a clear gradient with respect to the S_{23} emission line ratio. The absence of a clear gradient at higher metallicities may be because S_{23} is double-valued with respect to metallicity and is quite dependent on ionization parameter (Kewley & Dopita 2002). However, we also find that data points with extremely low values of S_{23} clearly show harder radiation field lying between the constant values of log $\eta' = -0.5$ to 0. Those data points (lying in the top right corner of middle panel) are predominantly from the central region of an SF galaxy (Manga-8626-12704, see Fig. D7), which shows prominent detection of the auroral line [O III] λ4363. The detection of this weak emission line and the range of electron temperatures (Fig. D7, lower right-hand panel) show that the metallicities of these data points are low. Hence, in spite of the degeneracies related to the ionization parameter and double-valued nature of S_{23}, this plot is consistent with an inverse relation between metallicity and hardness of radiation field.

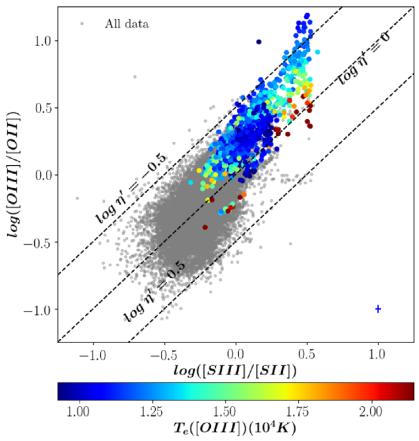

Figure 5. Spatially resolved data of all 67 galaxies plotted on O_3O_2–S_3S_2 plane, where coloured data points have T_e([O III]) measurements while grey data points indicate the entire data set. The diagonal dashed lines represent the constant values of log $\eta' = -0.5$, 0, 0.5. The typical uncertainties on both axes (i.e. O_3O_2 and S_3S_2) are shown in the lower right corner while the typical uncertainty on T_e([O III]) is given as σ in the upper left corner of each panel.

In summary, we conclude that the gas-phase metallicity depends on the radiation hardness as traced by log η' (on O_3O_2–S_3S_2 plane), i.e. low-metallicity gas is associated with harder radiation field and vice versa. This result agrees with those of Kehrig et al. (2006), who found that H II regions with lower gaseous metallicity present harder ionizing spectra. Kewley et al. (2013) pointed out several potential reasons, which might cause the correlation between metallicity and radiation hardness. However, the diagnostics of metallicity and ionization parameter are correlated as well (Dopita & Evans 1986; Pérez-Montero 2014), as such radiation hardness might be related to ionization parameter.

3.2 Electron temperature (T_e([O III])) and density (N_e)

Fig. 5 shows O_3O_2–S_3S_2 plane where data points are colour-coded with respect to electron temperature T_e([O III]). We estimated T_e([O III]) on a spaxel-by-spaxel basis for all galaxies in the sample where auroral line [O III] λ4363 was detected with S/N > 3 by using the emission line ratio of ([O III] λλ4959, 5007)/[O III] λ4363 with the prescriptions given in Pérez-Montero (2017). We restrict our analysis of O_3O_2–S_3S_2 plane to only those spaxels with T_e([O III]) lying in the range of 7000–25000 K, as the involved equations are valid only in the above-mentioned range.[6] We find that the majority of data points lies in the range of log $\eta' = -0.5$ and 0. At first glance, it might appear that galaxies with [O III] λ4363 detection (and T_e([O III]) estimates) exhibit harder radiation fields, though model-based analysis shows no such relation (Fig. A1). The absence of data points with T_e measurements on the lower left corner in Fig. 5 is likely due to an overall lower O^{++}/O.

[6]We also estimated T_e([O III]) by using emission line fluxes in PYNEB (v1.1.14, Luridiana, Morisset & Shaw 2013) and did not find any significant difference in the overall trend.

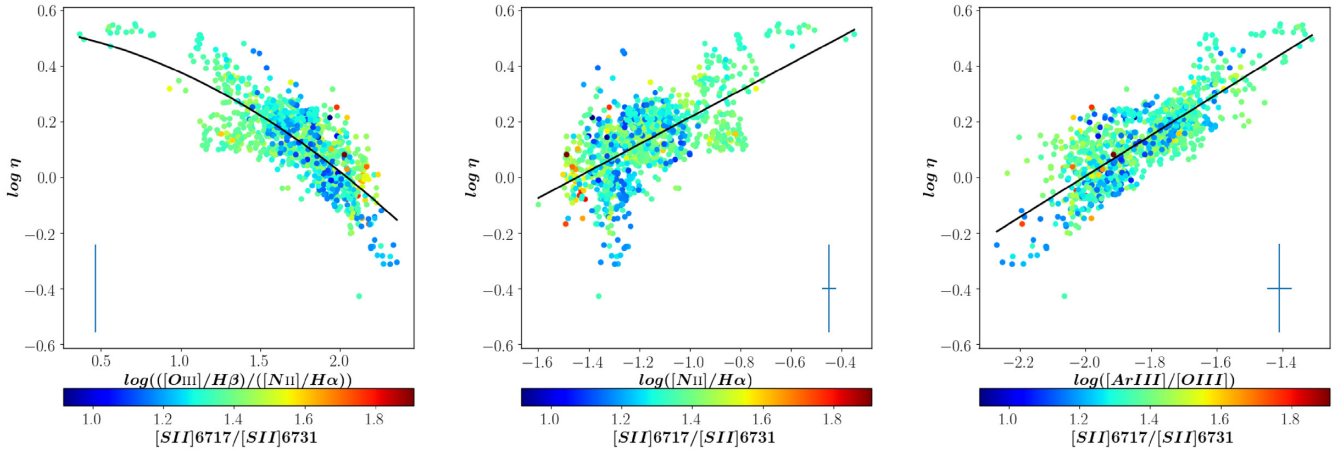

Figure 6. Relation between softness parameter (log η) and emission line ratios sensitive to the abundance, O_3N_2 (left-hand panel), N_2 (middle panel), and Ar_3O_3 (right-hand panel), where data are colour-coded with respect to N_e-sensitive [S II] doublet ratio. The median uncertainties on *x*-and *y*-axes are shown in the lower left corner of the left-hand panel and in the lower right corners of the other two panels. The median uncertainty on O_3N_2 is quite small. The solid black curve on each panel shows the best-fitting curve to the spatially resolved data points.

Vilchez & Pagel (1988) show that ionic quotient ratio log η varies directly with the oxygen abundance. We explore this further by estimating log η using O_3O_2, S_3S_2 and T_e([O III]) within equation (3) and study its variation with respect to the abundance-sensitive emission line ratio O_3N_2, N_2 and Ar_3O_3 as shown in Fig. 6. We find that softness parameter decreases with O_3N_2 but increases with N_2 and Ar_3O_3 implying that the hardness of radiation field varies proportionally with the metallicity traced by the three line ratios. The result agrees with that of Vilchez & Pagel (1988), who show an increase of softness parameter with the oxygen abundance. Since metal leads to cooling, we expect higher electron temperature for metal-poor gas. The result is in agreement with that in Section 3.1 where metallicity is found to have an inverse dependence on log η' at a given log $\mathcal{U}$.

In Fig. 6, we also fit the following polynomials between log η and abundance-sensitive line ratios O_3N_2, N_2, and Ar_3O_3 using an orthogonal distance regression and taking into account uncertainties on both axes:

$$\log \eta = (-0.096 \pm 0.014)O_3N_2^2 - (0.068 \pm 0.046)O_3N_2 + (0.540 \pm 0.035). \quad (16)$$

$$\log \eta = (0.483 \pm 0.016)N_2 + (0.698 \pm 0.019). \quad (17)$$

$$\log \eta = (0.734 \pm 0.015)Ar_3O_3 + (1.47 \pm 0.028). \quad (18)$$

The above equations will allow future studies to estimate log η from O_3N_2, N_2 and Ar_3O_3, which are ratio of strong emission lines, thus extending the study of radiation hardness even in the systems where the temperature-sensitive weak auroral lines (e.g. [O III] λ4363) are not detected. We do not claim that the line ratios O_3N_2, N_2, and Ar_3O_3 trace radiation hardness; however, they can be used to estimate log η because of their sensitivity to metallicity and probably ionization parameter. So, caution should be made while interpreting the log η as radiation hardness when estimated from O_3N_2, N_2, or Ar_3O_3. In principle, similar relations can be found between log η and other abundance-sensitive line ratios shown in Fig. 4. However, we do not attempt to fit such a relation of η with the line ratios R_{23} or S_{23} since both of them are bi-modal in metallicity. We do not use S_3O_3 as we establish in Section 3.1 that the variation of η' with S_3O_3 might be a systematic effect of using the emission lines ratios of similar ionization potentials [O II] and [S II] in the definition of log η'.

In Fig. 6, data are colour-coded with respect to line ratio [S II]λ6717/[S II]λ6731, which is sensitive to N_e, showing that there is no obvious relation between N_e and radiation hardness. The result is consistent with the theoretical definition of log η (equation 3), which does not show any first-order dependence on N_e. Furthermore, a majority of data exhibit the [S II] doublet line ratio corresponding to the N_e typical of H II regions, i.e. there is not much variation of N_e within our data set and hence no secondary effect is seen in log η. Our results are in agreement with Hunt et al. (2010), who find that N_e is not correlated with radiation hardness, which they measure by [O IV]/[S II] line ratio in their sample of dwarf galaxies.

Here, we do a qualitative analysis to infer whether T_e might be related to T_{eff} on the basis of previous studies, which suggest that log η' decreases with the increase in T_{eff} (e.g. Kennicutt et al. 2000; Pérez-Montero & Vílchez 2009; Pérez-Montero et al. 2019). Kennicutt et al. (2000) also find that T_{eff}[7] decreases with respect to the gas-phase metallicity in a given abundance range. Similarly, Hägele et al. (2006) argues that for a given stellar mass, stars of lower metallicity have higher effective temperature. Our work shows a low gas-phase metallicity or high T_e for low log η'. Hence, this might imply that the SF regions hosting hotter stars with harder ionizing radiation and lower stellar metallicity might have lower gas-phase metallicity, which results in higher electron temperatures.

3.3 Ionization parameter and equivalent effective temperature

Fig. 7 shows the relation between log η' and the emission line ratios sensitive to ionization parameter, S_3S_2 (upper panel) and O_3O_2 (lower panel), where data points are colour-coded with respect to EW(H β) and the Pearson correlation coefficient (ρ) is mentioned in the bottom left. We find no correlation between log η' and S_3S_2 (upper panel, $\rho = -0.06$) while log η' decreases with an increase in O_3O_2 (lower panel, $\rho = -0.75$). S_3S_2 and O_3O_2 depend on log $\mathcal{U}$ and T_{eff} differently. While S_3S_2 depends more on log $\mathcal{U}$, O_3O_2 depends more on T_{eff} (Pérez-Montero et al. 2019). Similarly, S_3S_2

[7]Kennicutt et al. (2000) uses the terminology $T_\star$ for T_{eff} when abundance is not within the calibrated range.

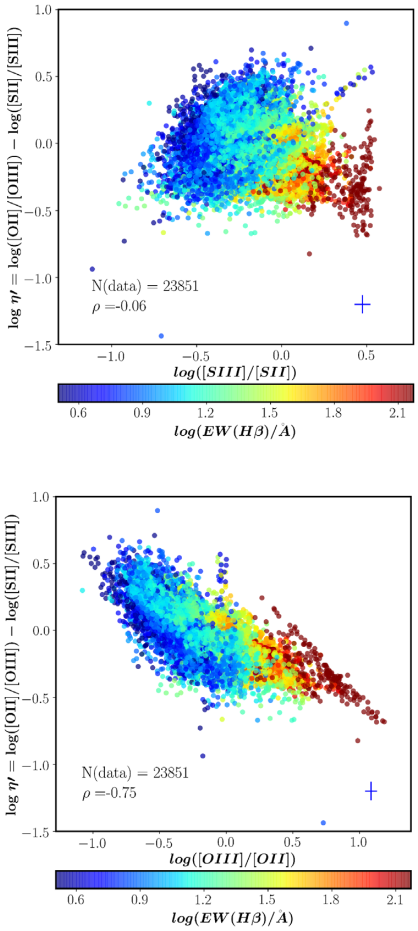

Figure 7. Relation between log η' and emission line ratios sensitive to the ionization parameter, S_3S_2 (upper panel) and O_3O_2 (lower panel), where data points are colour-coded with respect to EW(H β). The typical uncertainties on the variable on *x*- and *y*-axes are shown in the lower right corner. 'N(data)' represents the total number of plotted data points. ρ denotes the Pearson correlation coefficient.

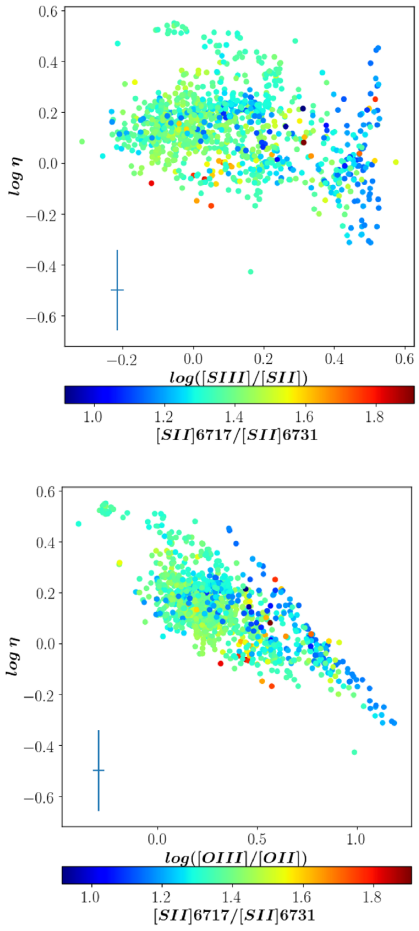

Figure 8. Relation between log η and emission line ratios sensitive to the ionization parameter, [S III]/[S II] (upper panel) and [O III]/[O II] (lower panel), where data are colour-coded with respect to N_e-sensitive [S II] doublet ratio. The typical uncertainties on the variable on *x*- and *y*-axes are shown in the lower left corner.

has been shown to be a better diagnostic of ionization parameter than O_3O_2 via CLOUDY photoionization models (Morisset et al. 2016). As such, no correlation of S_3S_2 and log η' might indicate that ionization parameter does not depend on radiation hardness as probed by log η'. A similar behaviour is seen in Fig. 8 where we compute log η using equation (3) and study its variation with respect to S_3S_2 (upper panel) and O_3O_2 (lower panel). However, we find in Section 3.1 that η and η' are correlated with strong line ratios such that N_2 and O_3N_2, which are sensitive not only to abundance but also to the ionization parameter. Hence, ionization parameter might be related to radiation hardness as well, as indicated by other works (see e.g. Pérez-Montero et al. 2020). We discuss this further in Section 4.1.

We explore this further in Fig. 9, which shows the relation between log η' and log $\mathcal{U}$ and colour-coded with respect to the equivalent effective temperature $T_{\rm eff}$. Both log $\mathcal{U}$ and $T_{\rm eff}$ are computed from the PYTHON-based code HCM-TEFF (v3.1)[8] (Pérez-Montero et al. 2019) using the direct-method metallicity and the emission line fluxes of [O II] λ3727, [O III]λ5007, [S II]λ6717, 6731, and [S III] λ9069. We find a lower value of log $\mathcal{U}$ for a higher value of log η' and vice versa, though error bars are large. Hence, an interdependence

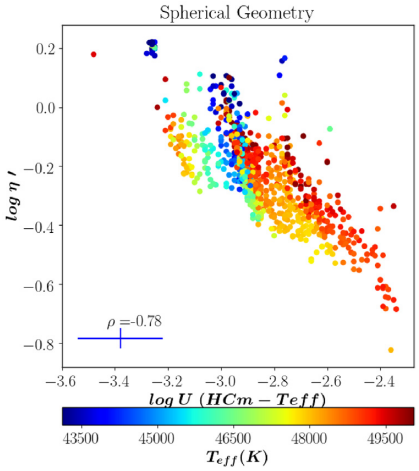

Figure 9. Relation between log η' and log $\mathcal{U}$ and colour-coded with respect to $T_{\rm eff}$ where log $\mathcal{U}$ and $T_{\rm eff}$ are determined from the code HCm-Teff for spherical geometry. ρ indicates the Pearson correlation coefficient. The typical uncertainties on the variable on *x*- and *y*-axes are shown in the lower left corner.

[8]https://www.iaa.csic.es/~epm/HII-CHI-mistry-Teff.html

between log $\mathcal{U}$ and log η' might be present. We discuss and explore this interdependence more via a comparison of data with models in Section 4.1.

However, we also note that $\mathcal{U}$, by definition, is not related to the shape of radiation field but the production rate of the Lyman continuum photons, distance from the stars or stellar clusters, and ionized or neutral hydrogen density. So, it is also possible that the emission line ratios S_3S_2 are rather tracing the ionization state of the gas, which is determined by factors including radiation hardness, $\mathcal{U}$ and optical depth (Ramambason et al. 2020).

In Fig. 9, we do not find any relation between log η' and equivalent effective temperature in contrast to the previous studies, which suggest that log η' decreases with an increase in $T_{\rm eff}$ for galactic and extragalactic H II regions (Kennicutt et al. 2000) and for the disc-averaged radial profiles of external galaxies (Pérez-Montero & Vílchez 2009). However, we cannot rule out such a dependence because the typical uncertainties on $T_{\rm eff}$ estimated from HCM–TEFF in our work is almost as large as the range of $T_{\rm eff}$.

We also studied the relation of log η with respect to equivalent effective temperature and ionization parameter, where the last two quantities were computed using HCm–Teff code as explained earlier. The trends are similar to that shown in Fig. 9. Note that the large errors on $T_{\rm eff}$ and lack of clear relation of log η or log η' with log $\mathcal{U}$ are likely due to the model grids used in HCM–TEFF (v3.1) based on single WM-Basic stars. We show later in Section 4.1 that model grids corresponding to older-age stellar populations satisfy MaNGA data set, which can be used with HCM–TEFF to study the relations of radiation hardness with log $\mathcal{U}$ and $T_{\rm eff}$.

3.4 Age of stellar populations

Fig. 10 shows O_3O_2–S_3S_2 plane where data points are colour-coded with respect to EW of H β (EW(H β)) (upper panel) and the narrow index of 4000 Å break (D_N(4000)) (lower panel), parameters sensitive to age of stellar populations.

EW(H β) measures the ratio of young ionizing population traced by H β emission line flux to the older non-ionizing population traced by the underlying continuum. As young and hot massive stars die, the supply of ionizing photons decreases, which depletes the nebular content of any hydrogen recombination lines (including H β), while the level of continuum is determined by long-lived, cooler lower-mass stars. Hence, EW(H β) decreases as the age of stellar population producing ionizing photons increases. As such, EW(H β) is a good diagnostic for starburst age and is used in various IFS studies but its use depends on assumption on various other parameters such as metallicity, initial mass function, stellar mass loss rates, and star formation history (Leitherer et al. 1999; Levesque & Leitherer 2013). For instantaneous star formation, EW(H β) is sensitive to stellar populations of ages up to 10 Myr (STRABURST99). In Fig. 10 (upper panel), we find that EW(H β) spans a range of ∼1–100 Å indicating that our sample includes SF regions with a variety of young stellar populations from relatively evolved to very recent starburst. However, our data do not show a clear correlation between EW(H β) and η', which might be partly due to the H β absorption. At high O_3O_2 and S_3S_2, we find the highest EW(H β), which corresponds to very young (∼3–5 Myr) stellar population. Most of these data points show η' lower than zero, suggesting a harder radiation field compared to the average η' of lower EW points, and hence indicate that the lower age stellar population are characterized by harder radiation field. The result is consistent with that of Kewley et al. (2001), who find that the ionizing spectrum becomes harder for lower age stellar population synthesis models of PEGASE V2.0

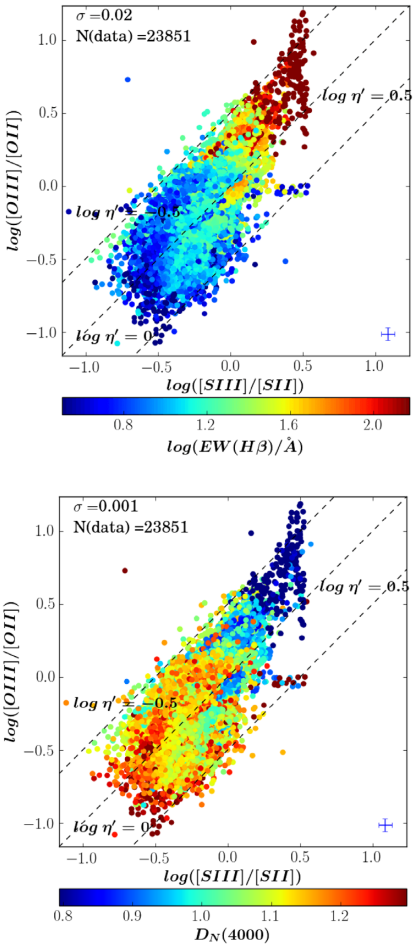

Figure 10. Spatially resolved data of all 67 galaxies plotted on O_3O_2–S_3S_2 plane, where data points are colour-coded with respect to log (EW(H β)) (upper panel) and D_N(4000) (lower panel). The diagonal dashed lines represent the constant values of log $\eta' = -0.5, 0, 0.5$. The typical uncertainties on O_3O_2 and S_3S_2 are shown in the lower right corner of each panel, while typical uncertainties on log (EW(H α)) and D_N(4000) are shown by σ in the upper left corner of upper and lower panels, respectively. 'N(data)' represents the total number of plotted data points.

(Fioc & Rocca-Volmerange 1997) and STARBURST99 (Leitherer et al. 1999). In Figs 7 and 10, we find high O_3O_2 and high S_3S_2 for high EW(H β) overall, consistent with Campbell, Terlevich & Melnick (1986), who find strong correlation between the O_3O_2 and EW(H β) in H II galaxies indicating that high ionization parameter might be related to younger stellar populations.

D_N(4000) represents the ratio of the narrow continuum bands (3850–3950 Å and 4000–4100 Å, Balogh et al. 1999) around the break occurring at 4000 Å, which is caused by a strongly changing opacity of stellar atmospheres at this wavelength. In hot O and B stars, metal ions exist in highly ionized state, which effectively decreases the opacity leading to weaker 4000-Å break than stars of other spectral types. As a result, old metal-rich galaxies have larger 4000-Å break than galaxies hosting younger stellar population. In Fig. 10 (lower panel), we find that a majority of data points have D_N (4000) lying in the range of 0.8–1.3 (i.e. at 99 per cent confidence interval) indicating relatively young stellar populations, i.e. ≲500 Myr (see e.g. Noll et al. 2009; Winter et al. 2010). We note here that unlike EW(H β), D_N (4000) is independent of metallicity up to an age of 1 Gyr. Furthermore, unlike EW(H β), D_N (4000) is sensitive to

underlying older stellar population, which might be co-spatial with the younger population traced by EW(H β). Despite such differences, both D_N (4000) and EW(H β) show a broadly consistent variation on the O_3O_2–S_3S_2 plane, i.e. younger regions [with higher EW(H β) and low D_N (4000)] seem to have higher ionization parameter (i.e. higher O_3O_2 and higher S_3S_2) at a given value of η'.

4 DISCUSSION

4.1 Comparison with photoionization models

In this section, we compare our observational results with predictions from photoionization models. The goal of this exercise is to provide a qualitative interpretation of the observed sulphur line ratios and discuss possible model limitations identified by previous works. In particular, some standard photoionization models appear to struggle in reproducing simultaneously high and low ionization lines observed in SF galaxies using both long-slit and IFU data. For example, Pérez-Montero & Vílchez (2009) and Kehrig et al. (2006) specifically showed that such models fail to explain the hardness of ionizing radiation of most low-mass SF galaxies in the O_3O_2–S_3S_2 plane. More recently, the shortcomings of photoionization models to reproduce sulphur ratios of a more general population of SF galaxies using MaNGA data have been addressed by Mingozzi et al. (2020), who suggest that this is due to limitations in the stellar atmosphere modelling and/or problems with sulphur line strengths due to inaccurate atomic data (see also Garnett 1989; Kewley et al. 2019, and references therein). While the sample used for the comparison performed by Mingozzi et al. (2020) is larger than that used in this work, the explored range of line ratios are actually very similar. For their comparison, they used four different models, which include those of Dopita et al. (2013); Levesque, Kewley & Larson (2010); Byler et al. (2017); and Pérez-Montero (2014). The best agreement with data was found to be the grid of CLOUDY photoionization models by Pérez-Montero (2014), though these models did not cover a significant fraction of the data analyzed by Mingozzi et al. (2020) and, in particular, the S_3S_2 ratio.

In order to explore these issues further, we have used the most recentCLOUDY v17.02 photoionization models available through the Mexican Million Models data base (3MdB, Morisset, Delgado-Inglada & Flores-Fajardo 2015). One of the improvements of CLOUDY v17.02 compared to previous versions is the inclusion of updated atomic parameters for sulphur, which is relevant to our study. Here, we use two sets of model grids, namely BOND-2 and CALIFA-2 in the 3MdB-17 data base[9] both of which adopt a SED obtained from the population synthesis code PopStar (Mollá, García-Vargas & Bressan 2009) for a Chabrier (2003) stellar IMF between 0.5 and 100 $M_\odot$. BOND-2 is an extension of the model grids developed for the code BOND (Bayesian Oxygen and Nitrogen abundance Determinations, Vale Asari et al. 2016) for the starburst age going up to 6 Myr and is used to derive oxygen and nitrogen abundances simultaneously in giant H II regions. On the other hand, CALIFA-2 is an extension of the model grids devised for the analysis of CALIFA galaxies (Cid Fernandes et al. 2013) and additionally uses the STARLIGHT spectral base of simple stellar populations of up to several Gyr (Cid Fernandes et al. 2014). The combination of BOND and CALIFA models spans a wide range in gas-phase metallicity of

[9]The full 3MdB data base, including these models, is documented and can be accessed at https://sites.google.com/site/mexicanmillionmodels/

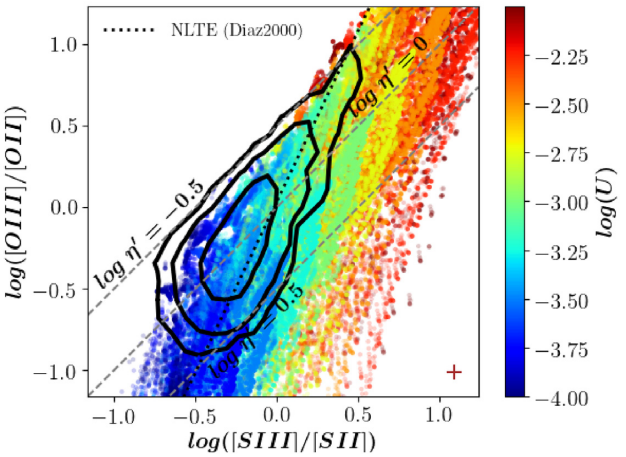

Figure 11. Photoionization models (colour points and black dotted lines) and spatially resolved data (grey contours) represented on the O_3O_2–S_3S_2 plane, where we have overlaid the three dashed lines corresponding to constant values of log $\eta' = -0.5$, 0, and 0.5. Inner to outer contours represent the 68 per cent, 95 per cent, and 99.7 per cent of the data points shown in Fig. 4, respectively. Both BOND and CALIFA models (see text for details) are colour-coded by the ionization parameter. The solid black line corresponds to equation (A1) and derived from the models of Díaz et al. (2000).

$\sim$0.01–1.5 solar, log $\mathcal{U}$ between -4 and -1.5, log(N/O) between -2 and 0.5, and a fixed electron density of 100 cm^{-3}.

In Fig. 11, we show the full set of BOND and CALIFA model predictions for the O_3O_2–S_3S_2 plane as a function of log $\mathcal{U}$. Overlaid, we display contours representing the 68 per cent, 95 per cent, and 99.7 per cent of the MaNGA spatially resolved data shown in Fig. 4. Additionally, we include non-LTE model predictions from Díaz et al. (2000), whose derivation is shown in Appendix A. We prefer here to show the full set of individual model predictions for each line ratio instead of the usual grid visualization in order to highlight differences and similarities with data and provide qualitative interpretations of our results. Finally, we note that shock models, which may affect the line ratios in complicated ways, have not been considered.

Conversely to previous works, the combination of model predictions from BOND and CALIFA does cover most data points in our sample. We note that this is mostly because of the inclusion of CALIFA models, as can be seen from the comparison shown in Figs A1–A4. The use of BOND models alone produces a systematic mismatch with nearly half of the spaxels, which is removed when CALIFA models are adopted. Moreover, in Fig. 11 the mean relations obtained from Díaz et al. (2000) models match the data relatively well, but a slight offset in the models towards higher S_3S_2 is apparent.

One of the main differences between the BOND and CALIFA models is the age of the ionizing stellar populations. In the former, this is restricted to OB stars in their first 6 Myr, while the latter includes aged stellar populations of up to several Gyr, which contribute to lower ionization regions (see e.g. Morisset et al. 2016). While such older age stellar population are generally found in the early-type galaxies with only a few or negligible H II regions, it is also possible that there is an underlying older stellar population along with the young stellar population within the galaxies under study. For example, a few galaxies in our sample are blue compact dwarfs, which are known to host both young and old stellar populations (see e.g. Aloisi et al. 2005; Amorín et al. 2009). Another possibility is the presence of hot low-mass evolved stars (HOLMES, Flores-Fajardo et al. 2011) with hard radiation fields as shown in Fig. A4 where lower EW(H β) and lower log(Q0/Q1) indicative of older

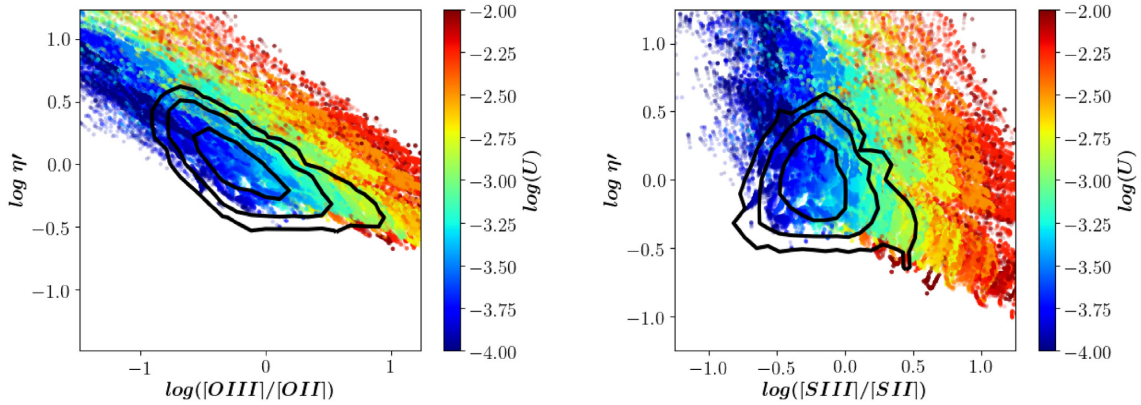

Figure 12. BOND and CALIFA photoionization models (colour points) and spatially resolved data (black contours) showing the relation between log η' and O_3O_2 (left-hand panel) and S_3S_2 (right-hand panel). Inner to outer contours represent the 68 per cent, 95 per cent, and 99.7 per cent of the data points shown in Fig. 7, respectively. Both BOND and CALIFA models (see text for details) are colour-coded by the ionization parameter.

stellar population tend to have relatively lower log η' indicative of harder radiation field. HOLMES might be associated with the low surface brightness regions and mostly have low log $\mathcal{U}$ and low log η' values, i.e. low O_3O_2 and low S_3S_2. As Fig. 11 shows, lower log $\mathcal{U}$ models match better with lower S_3S_2, whereas low O_3O_2 does not necessarily indicate low ionization parameter, probably pointing to secondary dependencies (e.g. metallicity; Kewley et al. 2019).

A good agreement between observations and models is also seen in Fig. 12, where we show the variation of log η' as a function of S_3S_2 (left-hand panel) and O_3O_2 (right-hand panel) and colour-coded with respect to log $\mathcal{U}$. This figure shows that the BOND and CALIFA models predict nearly all possible values of ionization parameter for a fixed value of log η'. This comparison also helps us to understand the observational trends seen in Fig. 7. The MaNGA data with higher EWs can be identified with models having both larger log $\mathcal{U}$ and harder radiation field (η'). Comparing the trends shown by S_3S_2 and O_3O_2, the former appears to be again a better diagnostic of the ionization parameter, less dependent of the hardness of the ionizing radiation. Moreover, Fig. 13 shows that S_3S_2 has a negligible relation with the metallicity-sensitive N_2 ratio in the models, in contrast to the O_3O_2 ratio. Similar trends are seen in the data. Therefore, S_3S_2 appears again as a more reliable tracer of log $\mathcal{U}$ than O_3O_2 as secondary dependencies with metallicity appear smaller.

The discrepancies found in previous works between data and models may come from a variety of factors. Models strongly rely on their simplified assumptions, such as the adopted geometry of the nebula (see Fig. 11), simplified temperature and density structure, or the uncertain atomic data for sulphur (e.g. Kewley et al. 2019). In the case of the line ratios under consideration, we find that models including the contribution to low ionization gas by aged stellar populations, in particular, HOLMES with hard radiation fields can significantly contribute to solve the discrepancies found by previous works relying on models in which the low and high ionization lines are powered only by very young stellar clusters (e.g. Mingozzi et al. 2020). Indeed, HOLMES have been proposed to explain line ratios sensitive to DIG in the past (e.g. Morisset et al. 2016), as these stellar populations can significantly contribute to increase the strength of some low ionization lines [SII] (Sanders et al. 2017). In Figs 11 and 12, we see that data showing low S_3S_2 and moderate-to-low O_3O_2 (i.e. relatively hard radiation field but low ionization parameter) related to the low-excitation gas can be better described with CALIFA models than BOND models, which seems to match better data with higher log $\mathcal{U}$ and higher log η' values (Figs A1 and A2 for a direct comparison).

Although we selected our data points to have [S III] detections and the contribution of DIG emission in our sample should not dominate in high EW data points probing high surface brightness regions (see examples of spatially resolved maps in Appendix D), the contribution of HOLMES is probably not negligible. This is especially true at low EW(H β) (characteristic of HOLMES), making the [S II] emission higher and therefore decreasing the S_3S_2 ratios in Fig. 12 compared to models. Similarly, there is likely an effect of underlying older stellar population in these young SF galaxies. We principally performed this analysis on spaxels with [S III] detection, some of which go beyond the maximum starburst line in Fig. 2 and hence could be affected by DIG. To rule out any effects in sample selection, we investigated only those data points that lie below the maximum starburst line on [S II]-BPT and found that there were still line ratios on O_3O_2–S_3S_2 plane, which could be explained by the older age CALIFA model grids but not the BOND model grids.

On the other hand, we do not see any significant mismatch between data and the BOND models in the S_3-N_2 and S_3-S_2 diagnostics presented in Fig. 3, which are also reproduced by the CALIFA models (see Appendix A, Fig. A1-A2). From these simple diagnostic, we can conclude that the S_3–S_2 plane (or the S_3S_2 ratio) is an excellent diagnostic for the ionization parameter, which shows a little dependence with metallicity (Fig. 13), as also shown by previous models (e.g. Kewley & Dopita 2002; Kewley et al. 2019).

Finally, we note that a recent approach to reconcile observed S_3S_2 and O_3O_2 ratios with models is presented by Ramambason et al. (2020), who show that classic photoionization models, like the ones we use in Figs 12 and 13, can underpredict the low-excitation line emission of [S II] arising from the outskirts of H II regions. To alleviate this, Ramambason et al. (2020) propose a composite model combining high and low ionization parameters, which is able to reconcile the S_3S_2 ratios of SF galaxies in SDSS using the same BONDS model grids adopted in our study. This is likely a much more reliable solution to model SF regions showing very high ionization, like the ones analyzed by Ramambason et al. (2020).

4.2 Comparison with previous works

In Fig. 14, we study the O_3O_2–S_3S_2 plane where we compare spatially resolved data from this study (brown points) with published data from literature, including H II regions along with global data of

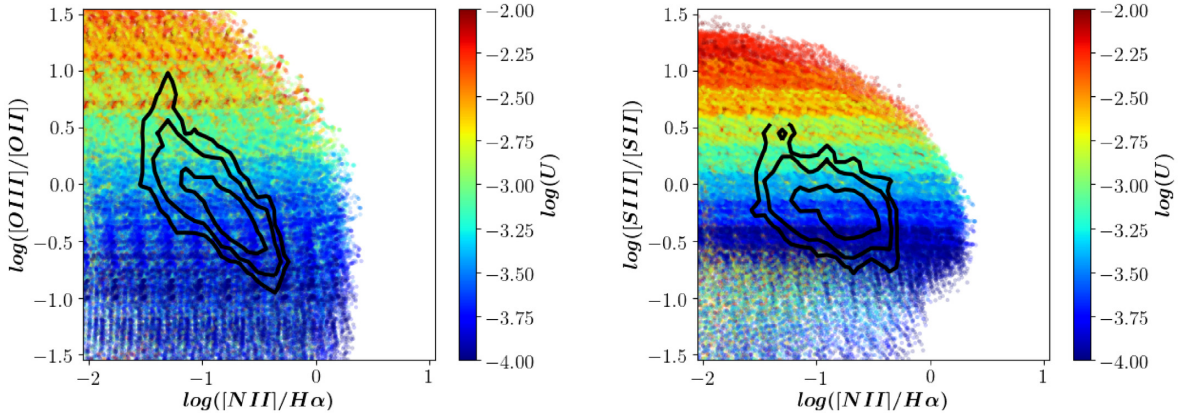

Figure 13. BOND and CALIFA photoionization models (colour points) and spatially resolved data (black contours) showing the O_3O_2 (left-hand panel) and S_3S_2 (right-hand panel) ratios as a function of N_2. Inner to outer contours represent the 68 per cent, 95 per cent, and 99.7 per cent of the data points shown in Fig. 4, respectively. Both BOND and CALIFA models (see text for details) are colour-coded by the ionization parameter.

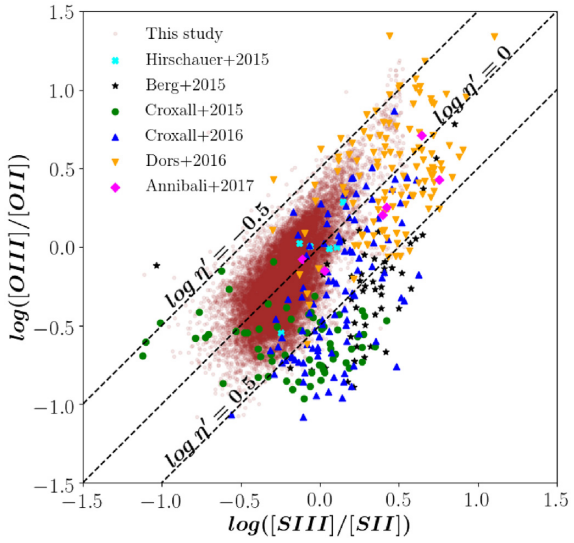

Figure 14. O_3O_2–S_3S_2 plane where we compare spaxel-by-spaxel MaNGA data from this study with published data of star-forming galaxies and H II regions within star-forming galaxies. We have overlaid the three dashed lines corresponding to constant values of log $\eta' = -0.5$, 0, and 0.5.

emission line galaxies. Table 2 shows data from literature along with references.

We find that H II regions from the nearby blue compact dwarf galaxy NGC 4449 (Annibali et al. 2017) are close to log $\eta' = 0$. The sample of Dors et al. (2016) consists of H II regions and SF galaxies and lies within the same range of log η' as our spatially resolved data, i.e. $-0.5 <$ log $\eta' < 0.5$. However, the majority of these data set have comparatively higher values of O_3O_2 and S_3S_2 than our spatially resolved data set. Since these two line ratios are sensitive to ionization parameter, it is possible that a large part of the sample of Dors et al. (2016) consists of objects with comparatively higher values of ionization parameter. We also find that all galaxies from Hirschauer et al. (2015) except one lie close to log $\eta' = 0$. We note that the galaxy from the sample of Hirschauer et al. (2015) with a relatively higher value of log η' has a relatively lower value of [O III] EW and higher metallicity compared to the other galaxies in their sample.

Table 2. References for the literature data plotted in Fig. 14.

Reference	Object
Berg et al. (2015)	NGC 0628 (H II regions)
Croxall et al. (2015)	NGC 5194 (H II regions)
Hirschauer et al. (2015)	Emission line galaxies
Croxall et al. (2016)	NGC 5457(H II regions)
Dors et al. (2016)	H II regions & galaxies[a]
Annibali et al. (2017)	NGC 4449 (H II regions)

[a]Compiled from Kennicutt et al. (2003), Vermeij & van der Hulst (2002), Hägele et al. (2008), Bresolin et al. (2009), Vílchez & Iglesias-Páramo (2003), Hägele et al. (2006), Hägele et al. (2011), Izotov et al. (2006), Guseva et al. (2011), Garnett et al. (1997), Vilchez & Pagel (1988), Skillman et al. (2013), López-Hernández et al. (2013), Zurita & Bresolin (2012), Pérez-Montero & Díaz (2003), Gonzalez-Delgado et al. (1995), Skillman & Kennicutt (1993), Russell & Dopita (1990), and Hägele et al. (2012).

In the case of spiral galaxies, NGC 0628 (black stars, Berg et al. 2015), NGC 5194 (green filled circles, Croxall et al. 2015), and NGC 5457 (blue triangles, Croxall et al. 2016), we find that a few H II regions lie within $-0.5 <$ log $\eta' < 0.5$ but a majority of H II regions tend to have higher values of log η' than average of our spatially resolved data. Spiral galaxies are known to present gradients in several physical properties. Pérez-Montero et al. (2019) studied the radial profiles of gas-phase metallicity, log η', log $\mathcal{U}$, and $T_{\rm eff}$ for these three galaxies using the same data set used here. For NGC 5194, they find that the H II regions in the central region ($< 4R_e$) of this galaxy show a drop in metallicity and have log $\eta' <0.5$, while the H II regions in the outskirts have higher log $\eta' > 0.5$ and near-solar metallicity. In Fig. 14, H II regions in NGC 5194 (green points) with log $\eta' < 0.5$ and sub-solar metallicity coincide with our sample. Hence, the offset of H II regions in spiral galaxies with respect to the MaNGA spatially resolved data on the O_3O_2–S_3S_2 plane in Fig. 14 indicates that our sample of predominantly irregular galaxies (and hence relatively lower gas-phase metallicities) has harder radiation fields on average compared to the higher-metallicity H II regions of CHAOS spiral galaxies. Pérez-Montero et al. (2019) also mention that there might be some relation of radiation hardness with log $\mathcal{U}$ and $T_{\rm eff}$ for which they suggest doing more detailed analysis. Furthermore, another possibility of the mismatch between MaNGA spatially resolved data and the overall location of H II regions can

be explained by the age of stellar populations. In Section 4.1, we find that the older stellar population included as ionization source in CALIFA model grids are necessary to match the MaNGA spatially resolved data, while Pérez-Montero et al. (2019) show that the H II regions within these spiral galaxies could be explained by the single star models.

While it is hard to clearly find the relation between radiation hardness and fundamental nebular properties, the analyses here show that the similarities and differences between MaNGA spatially resolved data and other data set shown in Fig. 14 are likely related to gas-phase metallicities with secondary dependence of other properties such as ionization parameter and age and equivalent effective temperature of stellar populations and possibly DIG.

4.3 Radiation hardness and helium ionization

The nebular helium emission is often associated with hard radiation fields (see e.g. Kehrig et al. 2015, 2018; Pérez-Montero et al. 2020; Senchyna et al. 2020). The He II λ4686 line can be produced only by the sources of hard ionizing radiation because the ionization potential of He II is very high (i.e. 54.4 eV). Such hard radiation can be produced by AGNs (Shirazi & Brinchmann 2012); stellar sources, such as cool white dwarf stars (Bergeron, Ruiz & Leggett 1997; Stasińska et al. 2008; Singh et al. 2013); hot WR stars (Schaerer 1996), shocks (Thuan & Izotov 2005), massive X-ray binaries (Garnett et al. 1991), post-AGB stars, (Binette et al. 1994; Papaderos et al. 2013), rapidly rotating, metal-free massive stars and/or binary population of very metal-poor massive stars (Kehrig et al. 2018). Given the importance of Helium detection in the context of hardness, we analyze seven galaxies separately here where He II 4686 was detected. These galaxies are marked with a † in Table 1, and relevant maps of this sample are shown in Section C. We have excluded two galaxies MaNGA-8250-3703 and MaNGA-8458-3702, in spite of He II λ4686 detection. The former is excluded because the He II emission in this galaxy shows the Wolf–Rayet (WR) bump, which is too broad to be considered as purely nebular. The latter is excluded because He II and H β are not co-spatial and as such prevents the analysis presented below.

Fig. 15 shows variation of He II λ4686/H β with [N II]/H α on a spaxel-by-spaxel basis in seven galaxies where He II λ4686 are detected. The solid black line corresponds to the maximum starburst line taken from Shirazi & Brinchmann (2012) and estimated from the Charlot & Longhetti (2001) models based on population synthesis codes of Bruzual & Charlot (2003) and CLOUDY photoionization models (Ferland 1996). On the original diagram of Shirazi & Brinchmann (2012), the region lying below the maximum starburst line corresponds to SF galaxies while the region beyond this line corresponds to H e II/H β values, which would require the contribution of some non-thermal ionization mechanism, such as an AGN. In Fig. 15, we have colour-coded data points with respect to the age diagnostic, EW(H β), which shows a smooth gradient going from SF part of the diagram to the AGN/composite part. The data points lying beyond the demarcation line belong to three different galaxies (manga-8549-6104, manga-8553-3704, and manga-8613-12703), and these spaxels are located on the edges of the brightest region in the H α map and have a relatively lower EW(H β). Since these spaxels do not coincide with the bright SF regions with high excitation but lie at their edges, it is possible that the enhanced He II/H β is due to the shocks (Thuan & Izotov 2005; Shirazi & Brinchmann 2012). However, an imperfect continuum subtraction might also be a problem as these spaxels with high He II/H β also have low EW(He II) (< 2 Å).

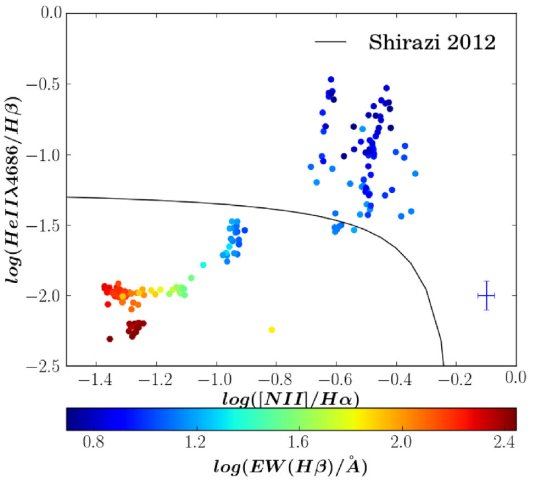

Figure 15. He II λ4686/H β versus [N II]/H α on a spaxel-by-spaxel basis for all galaxies in the sample where He II λ4686 was detected but no WR bump. These galaxies are marked with † in Table 1. The solid black curve represents the maximum starburst line taken from Shirazi & Brinchmann (2012) and was devised to separate the star-forming galaxies from the AGNs or composite objects.

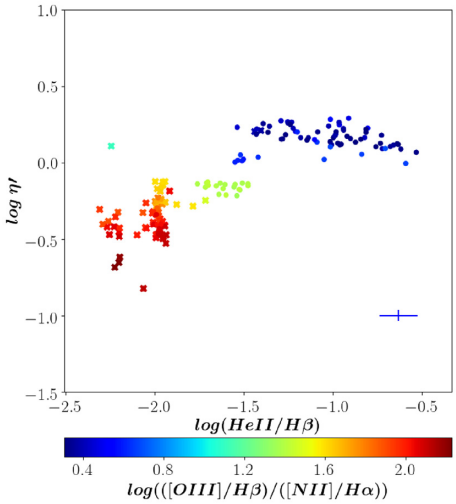

Figure 16. Relation between log η' and He II λ4686/Hβ, where data points are colour-coded with respect to abundance-sensitive line ratio O_3N_2. The typical uncertainties on the variable on *x*- and *y*-axes are shown in the lower right corner. 'N(data)' represents the total number of plotted data points. The data marked as stars have T_e([O III]) lying between 7000 and 25 000 K.

In Fig. 16, we study the relation between log η' and He II λ4686/Hβ[10] on a spaxel-by-spaxel basis for those galaxies where He II λ4686 is detected without any contamination by a WR broad stellar emission (see Table 1). log η' increases with He II λ4686/H β up to log He II λ4686/Hβ ~ -1.5, after which log η' becomes constant, suggesting that lower values of He II λ4686/H β correspond to harder radiation fields, contrary to the expectation that harder radiation field would result in nebular helium lines. Further tests need to be done on a larger sample of galaxies where nebular helium

[10]We could not do this experiment with other He lines because (i) He I 5876 overlapped with the Galactic sodium lines for one of the galaxies and (ii) He I 6678 was not detected with S/N > 3.

lines are detected. The data marked as stars have [O III] λ4363 detections and electron temperatures from the [O III] 43636/[O III] 5007 line ratio lie between 7000 and 25 000 K. The data points in this figure are colour-coded with respect to abundance-sensitive line ratio O_3N_2, thus showing a smooth increase in metallicity with increasing He II λ4686/H β and decreasing log η'. Though there is a strong dependence of O_3N_2 on the ionization parameter, we deem our choice of O_3N_2 to be the most appropriate here because the metallicity diagnostics such as R_{23} and O_3S_2 (Kumari et al. 2019; Maiolino & Mannucci 2019), which have only a secondary dependence on log $\mathcal{U}$, are also bimodal.

In this study, we could not map all optical helium lines (He I λ5876, He I λ6678, and He I λ7785), and He II λ4686 was detected only in a few spaxels. Deeper S/N data would help us to overcome challenges of this work for which ground-based GMOS-IFU would be extremely useful. A possible avenue to investigate this work further is to study the UV helium lines in low-metallicity local galaxies for which COS and STIS instruments on *HST* would be extremely useful. With the launch of JWST, we will be able to apply the findings from the ground-based optical studies and space-based UV studies to the high-z low-metallicity galaxies where harder ionization radiation fields are expected.

5 SUMMARY

In this paper, we used the IFS MaNGA data of 67 nearby ($0.02 \lesssim z \lesssim 0.06$) SF galaxies to explore the relation between radiation hardness and various properties encoded in the emission lines emanating from the ionized gas within SF galaxies. In particular, we studied in detail softness parameter (log η, Vilchez & Pagel 1988) by investigating the observable quantity log η', which is the ratio of the two emission line ratios, O_3O_2 and S_3S_2, accessible by the long wavelength range of MaNGA covering the NIR sulphur lines such as [S III] λλ 9069, 9532. In this analysis, we have considered various diagnostics sensitive to age, electron temperature, metallicity, and ionization parameter in addition to exploring available models for explaining the observations. The main findings of this work are summarized below:

(i) We find that log η' is correlated to strong line metallicity diagnostics such as O_3N_2, N_2, Ar_3O_3, S_3O_3, R_{23}, and S_{23}. So, softness parameter, and consequently hardness of radiation fields, can be directly related to metallicity of ionized gas. We provide polynomial relations between log η and abundance-sensitive strong line ratios such as O_3N_2, N_2, and Ar_3O_3, which will allow us to study radiation hardness in galaxies where temperature-sensitive faint auroral lines are not detected, thus preventing to estimate softness parameter from its definition. We caution here not to use these relations for high-metallicity spiral galaxies, which are systematically offset with respect to the low-metallicity galaxies ($7.12 < 12+\log(O/H) < 8.6$) from which these relations are derived.

(ii) We do not find any particular trend on the S_3S_2–O_3O_2 plot with respect to age diagnostics [EW(H β) and D_N (4000)], though there are signatures of harder radiation field for lower EW(H β). Similarly, we do not find direct evidence of a relation between radiation hardness and ionization parameter and equivalent effective temperature, but such possibilities cannot be completely ruled out. No correlation is found between radiation hardness and electron density.

(iii) We compare the spatially resolved data with predictions from two publicly available CLOUDY (v.17) photoionization models, which allow us to study the relation between the stellar age and radiation hardness. Photoionization models including both young and evolved stellar populations are able to predict the observed line ratios indicating that the hot and old low-mass stars such as HOLMES and underlying older stellar population in the SF galaxies might also be associated with hard radiation fields.

(iv) We compared the MaNGA data with published O_3O_2 and S_3S_2 emission line ratios for SF galaxies and H II regions within SF galaxies and compared them with MaNGA data set from this work. We find that higher-metallicity H II regions within CHAOS spiral galaxies have on average higher softness parameter than the relatively lower-metallicity MaNGA SF galaxies studied here.

(v) Helium is generally associated with the harder radiation fields; hence, we explored the relation between log η' and He II/H β in seven galaxies of our sample where He II λ4686 is detected. We find that regions with softer ionizing radiation (i.e. higher η') with helium detection tend to have higher He II/H β ratios, higher metallicity, and lower EW(H β), and might be related to shocks.

Finally, the results of this study are useful in investigating the radiation hardness in high-z low-metallicity galaxies targeted by future ground- and space-based telescopes such as James Webb Space Telescope (JWST) and European Extremely Large Telescope. This work is crucial in preparation for the upcoming high-z surveys exploiting the outstanding NIR facilities such as Near-Infrared Spectrograph (NIRSPec) on JWST and Multi Object Optical and Near-infrared Spectrograph (MOONS) on Very Large Telescope (VLT). These future surveys will provide access to [S III] lines for galaxies at intermediate and high redshifts; hence, it is important to probe the usefulness of line ratios involving sulphur lines in local galaxies as potentially useful tracers of hardness, ionization, and metallicity. Moreover, the detailed spatially resolved analysis of radiation hardness will further aid in understanding the extreme conditions in high redshift galaxies, which host harder ionizing radiation (Stark et al. 2015).

ACKNOWLEDGEMENTS

We thank the referee for a thorough and constructive report and for providing us with equation (3). We also thank Claus Leitherer for a related discussion. NK acknowledges financial support from the Schlumberger Foundation, which facilitated her stay at the KICC during which a majority of work was carried out. RA acknowledges support from FONDECYT (Fondo Nacional de Desarrollo Científico y Tecnológico) regular grant 1202007. RM acknowledges ERC (European Research Council) advanced grant 695671 'QUENCH' and support by the Science and Technology Facilities Council (STFC). This project makes use of the MaNGA-Pipe3D data products. We thank the IA-UNAM MaNGA team for creating this catalogue, and the ConaCyt-180125 project for supporting them (Sánchez et al. 2016b). This research made use of Marvin, a core PYTHON package and web framework for MaNGA data, developed by Brian Cherinka, José Sánchez-Gallego, Brett Andrews, and Joel Brownstein (Cherinka et al. 2019); SAOImage DS9, developed by Smithsonian Astrophysical Observatory; and Astropy, a community-developed core PYTHON package for astronomy (Astropy Collaboration 2013).

DATA AVAILABILITY

The data used in this work form part of the MaNGA DR14 Pipe3D value-added catalogue (Sánchez et al. 2016a,b,c) and are publicly

available at https://www.sdss.org/dr14/manga/manga-data/manga-pipe3d-value-added-catalog/.

REFERENCES

Aloisi A., van der Marel R. P., Mack J., Leitherer C., Sirianni M., Tosi M., 2005, ApJ, 631, L45
Amorín R., Aguerri J. A. L., Muñoz-Tuñón C., Cairós L. M., 2009, A&A, 501, 75
Amorín R. O., Pérez-Montero E., Vílchez J. M., 2010, ApJ, 715, L128
Annibali F. et al., 2017, ApJ, 843, 20
Astropy Collaboration, 2013, A&A, 558, A33
Baldwin J. A., Phillips M. M., Terlevich R., 1981, PASP, 93, 5
Balogh M. L., Morris S. L., Yee H. K. C., Carlberg R. G., Ellingson E., 1999, ApJ, 527, 54
Belfiore F. et al., 2016, MNRAS, 461, 3111
Berg D. A., Skillman E. D., Croxall K. V., Pogge R. W., Moustakas J., Johnson-Groh M., 2015, ApJ, 806, 16
Bergeron P., Ruiz M. T., Leggett S. K., 1997, ApJS, 108, 339
Binette L., Magris C. G., Stasińska G., Bruzual A. G., 1994, A&A, 292, 13
Bresolin F., Kennicutt Robert C. J., Garnett D. R., 1999, ApJ, 510, 104
Bresolin F., Gieren W., Kudritzki R.-P., Pietrzyński G., Urbaneja M. A., Carraro G., 2009, ApJ, 700, 309
Bruzual G., Charlot S., 2003, MNRAS, 344, 1000
Bundy K. et al., 2015, ApJ, 798, 7
Byler N., Dalcanton J. J., Conroy C., Johnson B. D., 2017, ApJ, 840, 44
Campbell A., Terlevich R., Melnick J., 1986, MNRAS, 223, 811
Cardamone C. et al., 2009, MNRAS, 399, 1191
Chabrier G., 2003, PASP, 115, 763
Charlot S., Longhetti M., 2001, MNRAS, 323, 887
Cherinka B. et al., 2019, AJ, 158, 74
Cid Fernandes R. et al., 2013, A&A, 557, A86
Cid Fernandes R. et al., 2014, A&A, 561, A130
Croxall K. V., Pogge R. W., Berg D. A., Skillman E. D., Moustakas J., 2015, ApJ, 808, 42
Croxall K. V., Pogge R. W., Berg D. A., Skillman E. D., Moustakas J., 2016, ApJ, 830, 4
Curti M., Cresci G., Mannucci F., Marconi A., Maiolino R., Esposito S., 2017, MNRAS, 465, 1384
Díaz A. I., Pérez-Montero E., 2000, MNRAS, 312, 130
Diaz A. I., Pagel B. E. J., Wilson I. R. G., 1985, MNRAS, 212, 737
Diaz A. I., Terlevich E., Vilchez J. M., Pagel B. E. J., Edmunds M. G., 1991, MNRAS, 253, 245
Díaz A. I., Castellanos M., Terlevich E., Luisa García-Vargas M., 2000, MNRAS, 318, 462
Dopita M. A., Evans I. N., 1986, ApJ, 307, 431
Dopita M. A., Sutherland R. S., Nicholls D. C., Kewley L. J., Vogt F. P. A., 2013, ApJS, 208, 10
Dors O. L., Pérez-Montero E., Hägele G. F., Cardaci M. V., Krabbe A. C., 2016, MNRAS, 456, 4407
Falcón-Barroso J., Sánchez-Blázquez P., Vazdekis A., Ricciardelli E., Cardiel N., Cenarro A. J., Gorgas J., Peletier R. F., 2011, A&A, 532, A95
Feltre A., Charlot S., Gutkin J., 2016, MNRAS, 456, 3354
Ferland G. J., 1996, University of Kentucky Internal Report,
Fernández-Martín A., Pérez-Montero E., Vílchez J. M., Mampaso A., 2017, A&A, 597, A84
Fernández V., Terlevich E., Díaz A. I., Terlevich R., Rosales-Ortega F. F., 2018, MNRAS, 478, 5301
Fioc M., Rocca-Volmerange B., 1997, A&A, 500, 507
Fischer C. F., Tachiev G., Irimia A., 2006, At. Data Nucl. Data Tables, 92, 607
Fitzpatrick E. L., 1986, AJ, 92, 1068
Flores-Fajardo N., Morisset C., Stasińska G., Binette L., 2011, MNRAS, 415, 2182
Garnett D. R., 1989, ApJ, 345, 282
Garnett D. R., Kennicutt R. C., Jr, Chu Y.-H., Skillman E. D., 1991, ApJ, 373, 458
Garnett D. R., Shields G. A., Skillman E. D., Sagan S. P., Dufour R. J., 1997, ApJ, 489, 63
Goddard D. et al., 2017, MNRAS, 466, 4731
Gonzalez-Delgado R. M., Perez E., Diaz A. I., Garcia-Vargas M. L., Terlevich E., Vilchez J. M., 1995, ApJ, 439, 604
Gunn J. E. et al., 2006, AJ, 131, 2332
Guseva N. G., Izotov Y. I., Stasińska G., Fricke K. J., Henkel C., Papaderos P., 2011, A&A, 529, A149
Hägele G. F., Pérez-Montero E., Díaz Á. I., Terlevich E., Terlevich R., 2006, MNRAS, 372, 293
Hägele G. F., Díaz Á. I., Terlevich E., Terlevich R., Pérez-Montero E., Cardaci M. V., 2008, MNRAS, 383, 209
Hägele G. F., García-Benito R., Pérez-Montero E., Díaz A. I., Cardaci M. V., Firpo V., Terlevich E., Terlevich R., 2011, MNRAS, 414, 272
Hägele G. F., Firpo V., Bosch G., Díaz Á. I., Morrell N., 2012, MNRAS, 422, 3475
Hirschauer A. S., Salzer J. J., Bresolin F., Saviane I., Yegorova I., 2015, AJ, 150, 71
Hunt L. K., Thuan T. X., Izotov Y. I., Sauvage M., 2010, ApJ, 712, 164
Izotov Y. I., Schaerer D., Blecha A., Royer F., Guseva N. G., North P., 2006, A&A, 459, 71
Kauffmann G. et al., 2003, MNRAS, 346, 1055
Kehrig C., Vílchez J. M., Telles E., Cuisinier F., Pérez-Montero E., 2006, A&A, 457, 477
Kehrig C., Vílchez J. M., Pérez-Montero E., Iglesias-Páramo J., Brinchmann J., Kunth D., Durret F., Bayo F. M., 2015, ApJ, 801, L28
Kehrig C., Vílchez J. M., Guerrero M. A., Iglesias-Páramo J., Hunt L. K., Duarte-Puertas S., Ramos-Larios G., 2018, MNRAS, 480, 1081
Kennicutt R. C., Jr, Bresolin F., French H., Martin P., 2000, ApJ, 537, 589
Kennicutt R. C., Jr et al., 2003, PASP, 115, 928
Kewley L. J., Dopita M. A., 2002, ApJS, 142, 35
Kewley L. J., Dopita M. A., Sutherland R. S., Heisler C. A., Trevena J., 2001, ApJ, 556, 121
Kewley L. J., Groves B., Kauffmann G., Heckman T., 2006, MNRAS, 372, 961
Kewley L. J., Dopita M. A., Leitherer C., Davé R., Yuan T., Allen M., Groves B., Sutherland R., 2013, ApJ, 774, 100
Kewley L. J., Zahid H. J., Geller M. J., Dopita M. A., Hwang H. S., Fabricant D., 2015, ApJ, 812, L20
Kewley L. J., Nicholls D. C., Sutherland R. S., 2019, ARA&A, 57, 511
Kniazev A. Y., Pustilnik S. A., Grebel E. K., Lee H., Pramskij A. G., 2004, ApJS, 153, 429
Kumari N., Maiolino R., Belfiore F., Curti M., 2019, MNRAS, 485, 367
Law D. R. et al., 2015, AJ, 150, 19
Law D. R. et al., 2016, AJ, 152, 83
Leitherer C. et al., 1999, ApJS, 123, 3
Levesque E. M., Leitherer C., 2013, ApJ, 779, 170
Levesque E. M., Kewley L. J., Larson K. L., 2010, AJ, 139, 712
López-Hernández J., Terlevich E., Terlevich R., Rosa-González D., Díaz A., García-Benito R., Vílchez J., Hägele G., 2013, MNRAS, 430, 472
Luridiana V., Morisset C., Shaw R. A., 2013, Astrophysics Source Code Library, record ascl:1304.021
Maiolino R., Mannucci F., 2019, A&A Rev., 27, 3
Maiolino R. et al., 2008, A&A, 488, 463
Marino R. A. et al., 2013, A&A, 559, A114
Martín-Hernández N. L., Vermeij R., Tielens A. G. G. M., van der Hulst J. M., Peeters E., 2002, A&A, 389, 286
Mathis J. S., 1982, ApJ, 261, 195
Mathis J. S., 1985, ApJ, 291, 247
Mingozzi M. et al., 2020, A&A, 636, A42
Mollá M., García-Vargas M. L., Bressan A., 2009, MNRAS, 398, 451
Morisset C., Schaerer D., Bouret J.-C., Martins F., 2004, A&A, 415, 577
Morisset C., Delgado-Inglada G., Flores-Fajardo N., 2015, RMxAA, 51, 103
Morisset C. et al., 2016, A&A, 594, A37

Nakajima K. et al., 2018, A&A, 612, A94
Noll S., Burgarella D., Giovannoli E., Buat V., Marcillac D., Muñoz-Mateos J. C., 2009, A&A, 507, 1793
Osterbrock D. E., Ferland G. J., 2006, Astrophysics of Gaseous Nebulae and Active Galactic Nuclei. University Science Books, Sausalito, CA
Papaderos P. et al., 2013, A&A, 555, L1
Parikh T. et al., 2018, MNRAS, 477, 3954
Pérez-Montero E., 2014, MNRAS, 441, 2663
Pérez-Montero E., 2017, PASP, 129, 043001
Pérez-Montero E., Contini T., 2009, MNRAS, 398, 949
Pérez-Montero E., Díaz A. I., 2003, MNRAS, 346, 105
Pérez-Montero E., Díaz A. I., 2005, MNRAS, 361, 1063
Pérez-Montero E., Vílchez J. M., 2009, MNRAS, 400, 1721
Pérez-Montero E., García-Benito R., Vílchez J. M., 2019, MNRAS, 483, 3322
Pérez-Montero E., Kehrig C., Vílchez J. M., García-Benito R., Duarte Puertas S., Iglesias-Páramo J., 2020, A&A, 643, A80
Pettini M., Pagel B. E. J., 2004, MNRAS, 348, L59
Planck Collaboration XIII, 2016, A&A, 594, A13
Planck Collaboration XVI, 2014, A&A, 571, A16
Ramambason L., Schaerer D., Stasińska G., Izotov Y. I., Guseva N. G., Vílchez J. M., Amorín R., Morisset C., 2020, A&A, 644, A21
Russell S. C., Dopita M. A., 1990, ApJS, 74, 93
Sánchez S. F. et al., 2012, A&A, 538, A8
Sánchez S. F. et al., 2016a, RMxAA, 52, 21
Sánchez S. F. et al., 2016b, RMxAA, 52, 171
Sánchez S. F. et al., 2016c, A&A, 594, A36
Sánchez-Blázquez P. et al., 2006, MNRAS, 371, 703
Sanders R. L., Shapley A. E., Zhang K., Yan R., 2017, ApJ, 850, 136
Schaerer D., 1996, ApJ, 467, L17
Senchyna P., Stark D. P., Mirocha J., Reines A. E., Charlot S., Jones T., Mulchaey J. S., 2020, MNRAS, 494, 941
Shirazi M., Brinchmann J., 2012, MNRAS, 421, 1043
Singh R. et al., 2013, A&A, 558, A43
Skillman E. D., Kennicutt R. C., Jr, 1993, ApJ, 411, 655
Skillman E. D. et al., 2013, AJ, 146, 3
Smee S. A. et al., 2013, AJ, 146, 32
Stark D. P. et al., 2015, MNRAS, 454, 1393
Stasińska G., 2006, A&A, 454, L127
Stasińska G. et al., 2008, MNRAS, 391, L29
Stasińska G., Izotov Y., Morisset C., Guseva N., 2015, A&A, 576, A83
Steidel C. C. et al., 2014, ApJ, 795, 165
Thuan T. X., Izotov Y. I., 2005, ApJS, 161, 240
Vale Asari N., Stasińska G., Morisset C., Cid Fernandes R., 2016, MNRAS, 460, 1739
Vazdekis A., Sánchez-Blázquez P., Falcón-Barroso J., Cenarro A. J., Beasley M. A., Cardiel N., Gorgas J., Peletier R. F., 2010, MNRAS, 404, 1639
Vazdekis A., Ricciardelli E., Cenarro A. J., Rivero-González J. G., Díaz-García L. A., Falcón-Barroso J., 2012, MNRAS, 424, 157
Vermeij R., van der Hulst J. M., 2002, A&A, 391, 1081
Vilchez J. M., Esteban C., 1996, MNRAS, 280, 720
Vílchez J. M., Iglesias-Páramo J., 2003, ApJS, 145, 225
Vilchez J. M., Pagel B. E. J., 1988, MNRAS, 231, 257
Winter L. M., Lewis K. T., Koss M., Veilleux S., Keeney B., Mushotzky R. F., 2010, ApJ, 710, 503
Xiao L., Stanway E. R., Eldridge J. J., 2018, MNRAS, 477, 904
Yan R. et al., 2016, AJ, 152, 197
Zinchenko I. A., Dors O. L., Hägele G. F., Cardaci M. V., Krabbe A. C., 2019, MNRAS, 483, 1901
Zurita A., Bresolin F., 2012, MNRAS, 427, 1463

SUPPORTING INFORMATION

Supplementary data are available at *MNRAS* online.

Figures A1–A4.
Figures B1–B3.
Figures C1–C7.
Figures D1–D8.

Please note: Oxford University Press is not responsible for the content or functionality of any supporting materials supplied by the authors. Any queries (other than missing material) should be directed to the corresponding author for the article.

APPENDIX A: PHOTOIONIZATION MODELS

Figs A1–A4 show additional comparisons of photoionization models (BOND and CALIFA) and spatially resolved data in different parameter space, including O_3O_2 versus S_3S_2 (Fig. 4), and the novel emission line diagnostic diagrams (Fig. 3). These models are first presented in Fig. 11. In that figure, we also show model prediction (straight line) from Díaz et al. (2000) and is described below.

Díaz et al. (2000) used a large grid of single-star CLOUDY photoionization models (Ferland 1996), with non-local thermodynamic equilibrium (LTE) single-star stellar atmosphere models, closed geometry, and constant particle density, and derived the relation between log $\mathcal{U}$ and the emission line ratios sensitive to ionization parameter such as O_3O_2 and S_3S_2 (see equations 7 and 8 in Díaz et al. 2000). We combine the two equations to derive the following relation represented by the solid black line in Fig. 11:

$$O_3O_2 = 2.1\ S_3S_2 + 0.0375. \quad \text{(A1)}$$

We note that Díaz et al. (2000) discarded their relation of log $\mathcal{U}$-O_3O_2 as this formula underestimated the values of log $\mathcal{U}$ compared to other formulae for log U derived in their work.

APPENDIX B: SDSS CUTOUTS OF ALL 67 GALAXIES IN THE SAMPLE

Figs B1–B3 show the SDSS cutouts of all 67 galaxies in our sample where the magenta hexagon indicates the FOV of MaNGA and the horizontal green line indicates an angular scale of 5 arcsec. The four directions, north (N), south (S), east (E), and west (W) are shown as the vertical and horizontal green lines in the centre of each image. The MaNGA id is mentioned at the upper right corner of each cutout.

APPENDIX C: GALAXIES WITH HELIUM DETECTION

Figs C1–C7 present the relevant maps of those galaxies in our sample where helium is detected. These maps include those of Hα line flux, He II λ4686/Hβ, [O III] λ5007/Hβ, EW of Hβ, and softness parameter (all quantities in logarithmic).

APPENDIX D: GALAXIES WITH [O III] λ4363 DETECTION

Figs D1–D8 show the spatially resolved maps of several properties of galaxies with extended [O III] λ4363 detection. We have specifically chosen to show these data set because [O III] λ4363 detection allows us to determine T_e and hence log η, which is the proxy for radiation hardness. In addition, these figures also show the O_3O_2–S_3S_2 plane for each galaxy colour-coded with respect to parameters sensitive to abundance, T_e, and stellar age.

This paper has been typeset from a TEX/LATEX file prepared by the author.